Received: 8 May 2023 | Revised: 13 March 2024 | Accepted: 24 March 2024

DOI: 10.1002/qj.4728

Quarterly Journal of the Royal Meteorological Society RMetS

RESEARCH ARTICLE

Absolute instability of moisture-coupled waves on the equatorial beta-plane

Cameron G. MacDonald

Program in Atmospheric and Oceanic Science, Princeton University, Princeton, New Jersey, USA

Correspondence
Cameron G. MacDonald, Program in Atmospheric and Oceanic Science, Princeton University, Sayre Hall, 300 Forrestal Road, Princeton, NJ 08540, USA.
Email: cgm3@princeton.edu

Funding information
Cooperative Institute for Modeling the Earth System (CIMES), Princeton University/NOAA GFDL

Abstract

The instabilities produced by a linear model of the tropical atmosphere coupled to a prognostic equation for water vapour are investigated. The basic model with no meridional wind supports unstable eastward-propagating waves. For parameter regimes relevant to the Indo-Pacific warm pool, the long-time asymptotic behaviour of the unstable waves is found to be absolutely unstable, so that the amplitude of disturbances will grow in time at every point in the domain. The absolute instability of the system is realized at planetary length-scales and intraseasonal frequencies. Other parameter choices for the system do not produce this same behaviour at these length- and time-scales. It is shown that the resultant long-time behaviour of the instability is characterized by roughly equal roles for temperature and moisture fluctuations in setting the thermodynamic tendency of the waves. With the inclusion of momentum damping, the phase speed of the absolutely unstable solution is about 7 m·s^{-1}. Addition of a strong background meridional moisture gradient, as in recent studies on the Madden–Julian Oscillation (MJO), appears to remove the absolute instability from the system. In a background state that varies slowly in the zonal direction, it is shown analytically that localized regions of instability may be formed, again using parameter choices relevant to the warm pool. The dynamics and thermodynamics of these local instabilities show some correspondence with the observed development of the MJO as it propagates through the warm pool.

KEYWORDS

absolute instability, instability, Kelvin waves, Madden–Julian Oscillation, moist thermodynamics, tropical dynamics, waves

1 | INTRODUCTION

Significant challenges remain in the theory and modelling of equatorial waves in the troposphere (Jiang *et al.*, 2020; Kiladis *et al.*, 2009). It has been argued that inclusion of a prognostic equation for atmospheric water vapour in a shallow-water model allows for the emergence of linear waves with characteristics that can resemble those of observed low-frequency convectively coupled equatorial waves, the Madden–Julian Oscillation (MJO), and the Boreal Summer Intraseasonal Oscillation (Adames & Maloney, 2021; Neelin & Yu, 1994; Sobel *et al.*, 2001; Wang & Sobel, 2022a). Such models rely on moist convection to reduce the effective static stability felt by disturbances

---

in the Tropics to produce phase speeds much less than the dry gravity-wave speed (Emanuel *et al.*, 1994; Kiladis *et al.*, 2009). Additional modification of the effective stability by diabatic or advective processes is thought to be important for producing instability at planetary scales (Adames & Kim, 2016; Ahmed *et al.*, 2021; Inoue & Back, 2017; MacDonald & Ming, 2022). Under such conditions, it is possible for thermodynamics to be strongly influenced by fluctuations of moisture. This has led to the definition of "moisture modes", broadly referring to wave solutions in which moisture plays an important role, perhaps leading to phenomena with no direct analogue in a dry atmosphere (Adames & Maloney, 2021; Ahmed *et al.*, 2021).

The notion of the moisture mode has evolved significantly over time, and care must be taken to define specifically what is meant by the term. Previous works have discussed the historical development of these concepts (Adames & Maloney, 2021; Fuchs & Raymond, 2017). The moisture mode has been viewed in the literature as either any wave that carries a leading-order moisture signal (Fuchs & Raymond, 2017; Neelin & Yu, 1994) or, instead, the limiting behaviour of these waves in which variations of moist enthalpy are dominated by fluctuations in moisture (Adames *et al.*, 2019; Ahmed *et al.*, 2021; Mayta & Adames Corraliza, 2023). To avoid ambiguity, use of the term "moisture mode" in isolation will henceforth be avoided; the latter interpretation of the moisture mode is referred to as the "weak temperature gradient (WTG) moisture mode" for reasons that will become clear, with the term "quasi-equilibrium (QE) mode" used for waves that carry temperature and moisture signals of comparable magnitude, following Ahmed *et al.* (2021).

Theories of both WTG moisture modes and QE modes provide a relatively simple picture of the fundamental interactions between dynamics and convection that lead to the existence of the MJO (Adames & Kim, 2016; Ahmed, 2021). However, previous linear stability analyses of these waves have largely been concerned with the normal modes of the system and their corresponding temporal instability. The desire for analytical solutions means that most of these studies have been been limited to zonally uniform basic states. While some studies have explored the interaction between simple models of the MJO and a zonally asymmetric basic state (Majda & Stechmann, 2011; Raymond & Fuchs, 2009; Raymond & Fuchs, 2018), more theoretical work is needed on this topic.

Earth's zonal asymmetry limits the convective signal of the MJO primarily to the Indo-Pacific warm pool (WP), and the characteristics of the MJO change significantly as it propagates through the WP (Hendon & Salby, 1994; Mayta & Adames Corraliza, 2023). It was shown by Hendon and Salby (1994) that MJO initiation over the Indian Ocean is associated with planetary-scale temperature and heating anomalies that are roughly in phase, promoting growth of the disturbance, while over the Central Pacific the anomalies are more in quadrature. Furthermore, the thermodynamics of the MJO is controlled more by moisture in the Indian Ocean (Adames & Kim, 2016; Mayta & Adames Corraliza, 2023) and becomes more gravity-wave-like as the convectively active phase propagates into the Central Pacific (Mayta & Adames, 2023; Mayta & Adames Corraliza, 2023; Roundy, 2012a, 2012b; Sobel & Kim, 2012). Model experiments have shown that imposition of zonal asymmetries mimicking the WP can significantly enhance MJO-like variability (MacDonald & Ming, 2022; Maloney *et al.*, 2010). The mechanisms for the zonal development of the MJO and its gravity-wave transition also demand more theoretical investigation. From the standpoint of linear models for the MJO, these considerations necessitate a move beyond analysis of normal modes in uniform basic states.

In the study of linearly unstable flows, an important distinction must be made between systems that are absolutely unstable and those that are convectively unstable (The term convective instability in this context originates from plasma physics literature and has no connection to gravitational instability (Held, 2019)) (Briggs, 1964; Huerre & Monkewitz, 1985). As explained by Briggs (1964), absolute instabilities grow in amplitude at every point in space, while convective instabilities only grow in an envelope around the peak of the disturbance, eventually decaying at every point in space after sufficient time has passed. This concept has been well-studied in simple analogues of midlatitude flow (Farrell, 1982; Lin & Pierrehumbert, 1993; Merkine, 1977; Pierrehumbert, 1986; Simmons & Hoskins, 1979). Applying the theory set out by Briggs (1964), the pioneering work of Merkine (1977) showed that a two-level model on the midlatitude β-plane could support absolute instability. However, the ultimate conclusion of Lin and Pierrehumbert (1993) was that the typical midlatitude flow on Earth is not absolutely unstable in the presence of a westerly surface wind, and hence a localized storm track cannot sustain wave energy indefinitely, and instead requires disturbances to enter from upstream. The presence of absolute instability in a zonally varying flow is necessary for the development of localized, self-sustaining regions of instability (Huerre & Monkewitz, 1990; Pierrehumbert, 1984).

Recently, these concepts have been applied to the study of African easterly waves (Diaz & Aiyyer, 2015) and monsoonal disturbances (Rupp & Haynes, 2020). Diaz and Aiyyer (2015) showed that African easterly waves can disperse energy upstream, and are thus able to seed the growth of further wave crests without any external forcing. Rupp and Haynes (2020) related different regimes of monsoonal anticyclone flows—and in particular their propensity to shed eddies periodically—to the underlying absolute or convective instability of the associated linear problem in a shallow-water model. They further highlighted another important feature of absolutely unstable systems, namely their insensitivity to the specifics of an imposed forcing, provided the forcing is not growing in time at a rate faster than the absolute growth rate (Briggs, 1964).

In this study we will investigate the implications of absolute instability on equatorial waves when coupled to an equation for atmospheric water vapour. It will be shown that, in a uniform basic state, the emergent low-frequency unstable waves are in fact absolutely unstable. In the next section, we will develop the linear equations with which we will work and review the concepts of absolute and convective instability. Section 3 carefully identifies the nature of the instabilities in the system and shows that local instability is supported under certain parameter regimes. In Section 4, the instability of some alternative linear models for the tropical atmosphere is considered. A discussion of these results and their connection to the observed characteristics of the MJO is provided in Section 5. Finally, concluding remarks are given in Section 6.

2 | THEORETICAL BACKGROUND

2.1 | A linear model for the tropical atmosphere

The primitive equations on the equatorial β-plane linearized about a state of rest are given in pressure coordinates by

$$\frac{\partial \mathbf{v}}{\partial t} + \beta y \mathbf{k} \times \mathbf{v} + \nabla \phi = 0, \tag{1a}$$

$$\frac{\partial \phi}{\partial p} = -\frac{R_\mathrm{d} T}{p}, \tag{1b}$$

$$\nabla \cdot \mathbf{v} + \frac{\partial \omega}{\partial p} = 0, \tag{1c}$$

$$C_\mathrm{p} \frac{\partial T}{\partial t} + \omega \frac{\partial \bar{s}}{\partial p} = Q. \tag{1d}$$

The stratification is set by the vertical gradient of the basic-state dry static energy, $\partial \bar{s}/\partial p$, and all other notation is standard (Fulton & Schubert, 1985). In the absence of friction in the momentum equation, the system is closed except for the heating rate Q. The vertically integrated version of Equation (1d) is given by

$$C_\mathrm{p} \frac{\partial \langle T \rangle}{\partial t} + \left\langle \omega \frac{\partial \bar{s}}{\partial p} \right\rangle = \langle Q \rangle, \tag{2}$$

where $\langle \cdot \rangle$ represents a pressure integral from the surface to the tropopause. Rather than express $\langle Q \rangle$ in terms of the primitive variables, we introduce a prognostic equation for the column water vapour $\langle q \rangle$ of the atmosphere and write the heating rate as a function of $\langle q \rangle$ (Adames & Kim, 2016; Sobel & Maloney, 2012, 2013). The equation for $\langle q \rangle$ takes the form

$$\frac{\partial \langle q \rangle}{\partial t} = -\langle \mathbf{v} \cdot \nabla q \rangle - \left\langle \omega \frac{\partial q}{\partial p} \right\rangle + E - P, \tag{3}$$

where E is the evaporation from the ocean surface and P is the precipitation from the atmosphere. The latent heat of vapourization has been absorbed into $\langle q \rangle$, E, and P. The pressure velocity ω is then assumed to have separable vertical structure $\Lambda_\omega(p)$ of a first baroclinic mode, being zero at the surface and tropopause and attaining a maximum in the mid-troposphere. The momentum, continuity, and hydrostatic equations can then be used to relate the vertical structures of the other fields to Λ_ω. Such systems have been developed in a number of previous works (Adames *et al.*, 2019; Ahmed *et al.*, 2021; Fuchs & Raymond, 2017; Wang & Sobel, 2022b). After eliminating ω and T, the equations can be written as

$$\frac{\partial u_1}{\partial t} - \beta y v_1 + \frac{\partial \phi_1}{\partial x} = 0, \tag{4a}$$

$$\frac{\partial v_1}{\partial t} + \beta y u_1 + \frac{\partial \phi_1}{\partial y} = 0, \tag{4b}$$

$$-\frac{M_\mathrm{s}}{c^2} \frac{\partial \phi_1}{\partial t} = M_\mathrm{s} \left(\frac{\partial u_1}{\partial x} + \frac{\partial v_1}{\partial y} \right) + \frac{(1+r)}{\tau_\mathrm{c}} \langle q \rangle, \tag{4c}$$

$$\frac{\partial \langle q \rangle}{\partial t} = -M_q \left(\frac{\partial u_1}{\partial x} + \frac{\partial v_1}{\partial y} \right) - \frac{1}{\tau_\mathrm{c}} \langle q \rangle - A_q u_1 + B_q y v_1, \tag{4d}$$

where $(\cdot)_1$ indicates the horizontal structure of a field. Here $c = 50\,\mathrm{m \cdot s^{-1}}$ is the dry gravity-wave speed, $M_\mathrm{s} = \langle -\Lambda_\omega \partial_\mathrm{p} \bar{s} \rangle$ is an integrated measure of the dry stability of the atmosphere, $M_q = \langle \Lambda_\omega \partial_\mathrm{p} \bar{q} \rangle$ is a measure of the integrated moisture stratification, and τ_c is a convective relaxation time introduced by parametrizing the precipitation as $P = \langle q \rangle / \tau_\mathrm{c}$. The parameter r is a cloud–radiative feedback parameter, which relates radiative heating to precipitation, and A_q represents moistening processes such as wind–evaporation feedback, zonal advection of the mean moisture gradient, eddy moisture fluxes, and frictional convergence that are associated with the zonal wind (Adames *et al.*, 2019; Adames & Kim, 2016; Sobel & Maloney, 2013). Essentially, we have assumed that the moistening contribution from all of these terms can collectively be linearly related to the zonal wind perturbation. B_q is a meridional moisture advection parameter; as in Ahmed *et al.* (2021) and Wang and Sobel (2022a) we have assumed that the background meridional moisture gradient is linear in y.

A strong simplifying assumption can be made by neglecting the meridional wind entirely, that is, setting $v_1 = 0$. In the dry system, this approximation would filter all the equatorially trapped modes but for the Kelvin wave. With the inclusion of a prognostic moisture equation, some of the essential features of intraseasonal variability can still be captured (Adames *et al.*, 2019; Ahmed *et al.*, 2021; Fuchs & Raymond, 2017). The advantage of this approximation is that it greatly simplifies the interpretation of the results attained through the forthcoming asymptotic analysis; we shall return to the more general problem with non-zero meridional wind in Section 4.2.

We now seek normal mode solutions of the form $u_1 \propto e^{i(kx-\sigma t)}$, with wave number k and frequency σ. After setting $v_1 = 0$, Equations (4a) and (4b) may be combined to show that all the fields in the model have the meridional structure

$$\mathcal{P}(y) = \exp(-\beta k y^2/(2\sigma)). \tag{5}$$

It then follows that, for real $k > 0$, solutions with $\Re(\sigma) < 0$ will not be equatorially trapped and thus do not hold any physical relevance. Combining Equations (4a), (4c), and (4d) and eliminating ϕ_1 and $\langle q \rangle$ gives a governing equation for the system:

$$\left(\frac{\partial}{\partial t} + \frac{1}{\tau_c}\right)\frac{\partial^2 u_1}{\partial t^2} - c^2\frac{\partial^3 u_1}{\partial x^2 \partial t} - c^2\frac{\tilde{M}_e}{\tau_c}\frac{\partial^2 u_1}{\partial x^2} + c^2\frac{\tilde{A}_q}{\tau_c}\frac{\partial u_1}{\partial x} = 0, \tag{6}$$

where $\tilde{M}_e = (1+r)(1 - M_q/M_s) + r$ is the effective gross moist stability (GMS), and $\tilde{A}_q = (1+r)A_q/M_s$ is a rescaled moistening parameter with dimensions of inverse length (Adames *et al.*, 2019). The corresponding dispersion relation is given by

$$\tau_c \sigma^3 + i\sigma^2 - \tau_c c^2 k^2 \sigma - ic^2k^2(\tilde{M}_e + i\tilde{A}_q k^{-1}) = 0. \tag{7}$$

For waves with intraseasonal periods, the cubic term in σ is small relative to the quadratic term, since the convective time-scale τ_c (which is of the order of 1 day or less) is much faster than the time-scale of the waves (Adames & Kim, 2016). Wang and Sobel (2022b) have shown that, when τ_c is around 1 day, neglecting this term filters a Kelvin wave damped at the rate τ_c^{-1}. Adames *et al.* (2019) showed that, for a convective time-scale of 2 h and positive effective GMS, Kelvin waves that are unstable at planetary scales still exist under this approximation. The filtered mode becomes nearly stationary in this limit, remaining damped at the shortened convective time-scale (Ahmed *et al.*, 2021). We therefore interpret this approximation as removing the initial adjustment to a QE state. Since we are primarily concerned with asymptotic behaviour, this strongly damped mode is not of particular interest. The resulting dispersion relation is then

$$i\sigma^2 - \tau_c c^2 k^2 \sigma - ic^2k^2(\tilde{M}_e + i\tilde{A}_q k^{-1}) = 0. \tag{8}$$

Previous studies suggest that this simplification has minimal influence on the unstable modes of the system at planetary scales (Adames *et al.*, 2019; Wang & Sobel, 2022b). Had we also neglected the tendency of the geopotential in the governing equations, the resulting dispersion relation would be

$$\tau_c \sigma + i(\tilde{M}_e + i\tilde{A}_q k^{-1}) = 0. \tag{9}$$

Note that this choice is mathematically equivalent to the limit in which $c \to \infty$ in Equation (7). It is clear that in this limit $-\tilde{M}_e/\tau_c$ is the growth rate of the wave, and that the frequency of the wave depends on $\tilde{A}_q$. The resulting solutions are WTG moisture modes in the extreme sense that they have no temperature signal at all. This limit emerges from the strict application of the WTG hypothesis, in which gravity waves act infinitely fast to remove temperature perturbations (Bretherton & Smolarkiewicz, 1989).

The forthcoming analysis will also necessitate solving the dispersion relation for k as a function of given σ. Equation (8) may be written in powers of k as

$$-c^2(\tau_c\sigma + i\tilde{M}_e)k^2 + c^2\tilde{A}_q k + i\sigma^2 = 0. \tag{10}$$

It should be noted that $k(\sigma)$ still encodes the information of the dispersion relation, but supplies the *complex* wave number for a given complex frequency. Briggs (1964) provides an extensive discussion of this interpretation in terms of systems that are forced at a single complex frequency.

Solutions for $\sigma(k)$ using Equation (8) produce one root that is unstable at planetary scales. The other root has $\Re(\sigma) < 0$ for all real $k > 0$; in view of Equation (5), the corresponding meridional structure is not equatorially trapped and therefore this root merits no further discussion. Figure 1a shows the frequency of the unstable solution in three separate parameter regimes. The specific parameter values are summarized in Table 1. For large values of τ_c and small or negative values of $\tilde{M}_e$, the solution takes on the character of a QE mode (Ahmed *et al.*, 2021; Wang & Sobel, 2022b), while for small values of τ_c and large $\tilde{M}_e$ it behaves like a Kelvin wave.

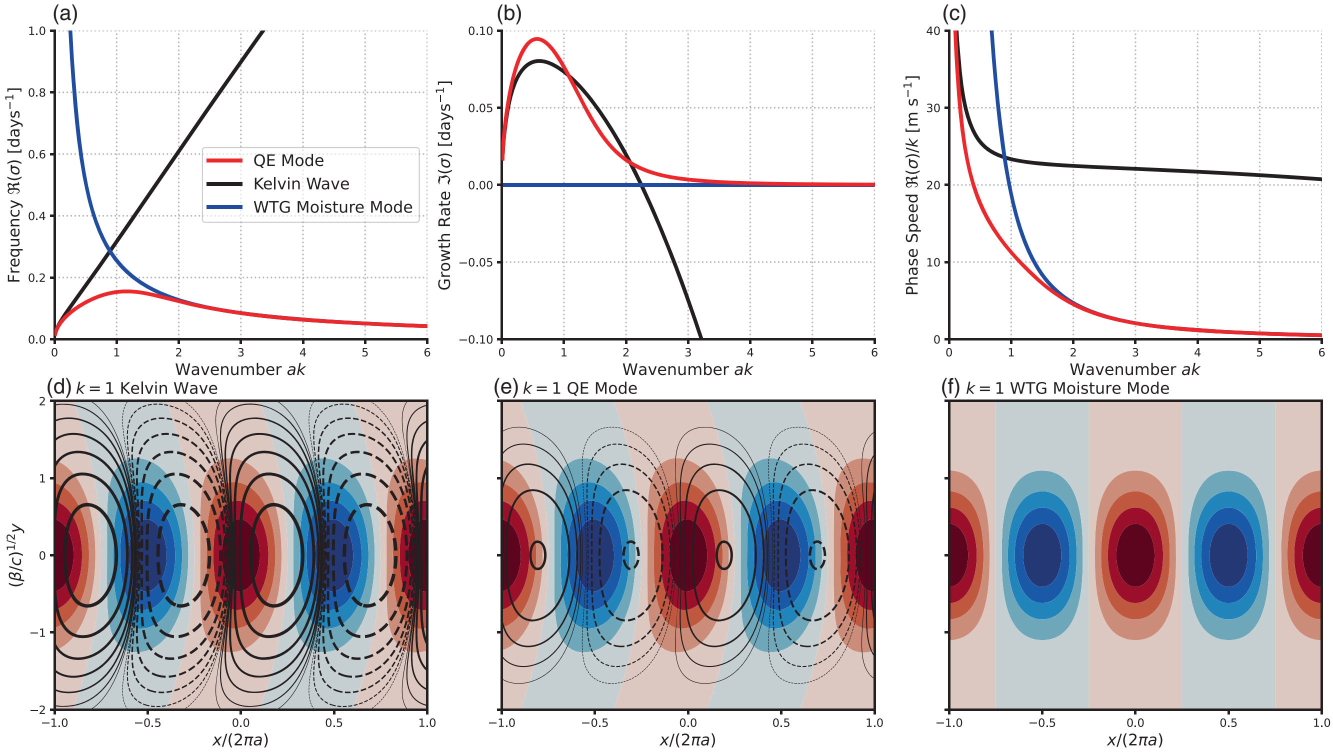

FIGURE 1 (a) Frequency $\Re(\sigma)$ of the unstable mode in the three different regimes for the system. Note that the linear frequency (the inverse of the period) is given by $\Re(\sigma)/2\pi$. (b) Growth rate $\Im(\sigma)$ of the unstable modes. (c) Phase speed $\Re(\sigma)/k$ of the unstable modes. (d) spatial structure of the $k = 1$ Kelvin mode for a unit perturbation of column water vapour $\langle q \rangle$ (shading). The contours show the corresponding column temperature perturbations $-M_s\phi_1/c^2$. The contours are in powers of 2, with the thinnest contours at $\pm 1/8$ and the thickest at ± 8. (e) As in (d) but for the QE regime. (f) As in (d) but for the WTG moisture-mode regime, in which temperature perturbations are negligible.

TABLE 1 Summary of parameter values used in the three different regimes shown in Figure 1. The value $c = \infty$ for the WTG moisture mode refers to the use of Equation (9) in place of Equation (8) as the dispersion relation.

Parameter	Kelvin wave	QE Mode	WTG moisture mode	Units
$\tilde{M}_e$	0.2	0	0	dimensionless
τ_c	2	12	12	hr
c	50	50	∞	m·s^{-1}
$\tilde{A}_q$	2×10^{-8}	2×10^{-8}	2×10^{-8}	m^{-1}

In the limit where the gravity-wave speed is made infinite, the solutions become WTG moisture modes, with thermodynamics controlled exclusively by moisture perturbations (Ahmed *et al.*, 2021). The Kelvin wave is essentially non-dispersive, while the frequency of the WTG moisture mode has a k^{-1} dependence, as seen from Equation (9); the QE mode is in some sense a smooth transition between these two regimes. This transition causes the QE regime to have a lower frequency at $k = 1$ than either of its limiting cases. The corresponding growth rates are shown in Figure 1b. Both the Kelvin wave and QE mode are unstable at planetary scales, while the growth rate of the WTG moisture mode takes on a constant value of $-\tilde{M}_e/\tau_c$. The phase speeds of the waves are shown in Figure 1c.

The horizontal structures of the planetary scale waves in each regime are shown in Figure 1d–f. For the Kelvin and QE modes, moisture and temperature are slightly in phase, indicating growth of wave variance, since the convective heating is proportional to moisture. The column temperature perturbations of the Kelvin wave are roughly an order of magnitude larger than the moisture perturbations, while for the QE mode the two fields are of similar magnitude. For the WTG moisture mode, the temperature perturbations are negligibly small relative to moisture, and instability requires a negative effective GMS so that the overturning circulation imports more moist static energy than it exports.

2.2 | Numerical methods

Numerical simulations will be performed to motivate the theoretical results derived from the dispersion relation. In these simulations, we allow the parameters of the model $\tilde{M}_{\mathrm{e}}$, τ_{c}, and $\tilde{A}_q$ to be spatially varying. The system governed by Equation (8) can be written as a first-order system in matrix form as

$$\frac{\partial}{\partial t}\begin{pmatrix}u_1\\ \dot{u}_1\end{pmatrix} = \begin{pmatrix}0 & 1\\ c^2\partial_x(\tilde{M}_{\mathrm{e}}\partial_x\cdot) - c^2\partial_x(\tilde{A}_q\cdot) & c^2\partial_x(\tau_{\mathrm{c}}\partial_x\cdot)\end{pmatrix}\begin{pmatrix}u_1\\ \dot{u}_1\end{pmatrix} + \begin{pmatrix}0\\ F\end{pmatrix}, \tag{11}$$

where $\dot{u}_1 = \partial_t u_1$ and F is a forcing term, which excites the system from an initial state of rest. The zonal coordinate is non-dimensionalized as $x = 2\pi a\hat{x}$, and time as $t = (\beta c)^{-1/2}\hat{t}$, where a is the radius of Earth. The forcing is given by

$$F(x,t) = \begin{cases} F_0\cos^2(\pi\hat{x})\delta(\hat{t}) & \text{if } |\hat{x}| < 1/2,\\ 0 & \text{otherwise,}\end{cases} \tag{12}$$

where F_0 is the amplitude of the forcing and $\delta(\cdot)$ is the Dirac delta function, that is, the forcing is only present for the first time step. The choice of forcing is rooted in the properties of the Fourier transform; its strongly peaked structure in both space and time is intended to excite all the wave numbers and frequencies of the system equally, so that the most unstable modes will quickly come to dominate the system. The spatial coordinate, which ranges from $\hat{x} = -20$ to $\hat{x} = 20$, is decomposed into 512 Fourier components. Terms that are the product of two spatially varying quantities are evaluated using the spectral transform method (Durran, 2013). The system is stepped forward in time using a third-order Adams–Bashforth scheme, with two initial fourth-order Runge–Kutta steps to initialize the time-stepping procedure. An additional ∂_x^4 diffusion term has been added to the system to remove energy at the smallest scales, but does not affect the behaviour appreciably at the scales of interest.

2.3 | Absolute and convective instability

We now review some essential points about the concepts of absolute and convective instability, closely following the discussion provided by Pierrehumbert (1984, hereafter P84). It is evident from the dispersion diagrams shown in Figure 1 that, outside the WTG moisture-mode limit, $\sigma_i > 0$ for some range of wave numbers, where $\sigma_i = \Im(\sigma)$. That is, the system is linearly unstable and the domain-integrated wave amplitude will grow in time. However, as stressed by P84, the existence of instability does not necessitate the growth of wave amplitude at every point in physical space. Consider a localized pulse disturbance that evolves in time according to the dispersion relation as

$$u_1(x,t) = \int_{-\infty}^{\infty} \mathcal{U}(k)e^{i[kx/t-\sigma(k)]t}\,dk, \tag{13}$$

where $\mathcal{U}(k)$ sets the initial shape of the pulse (in our numerical simulations, $\mathcal{U}(k)$ constitutes a discrete set of Fourier coefficients computed at some $t > 0$, i.e., after the initial forcing has turned off). To derive an asymptotic expression in the limit $t \to \infty$, it is assumed that, for large t, the argument of the exponential in Equation (13) varies much faster in k than $\mathcal{U}(k)$ does, and thus in general the variations over an entire phase will cancel out. However, this is not the case when the derivative of the phase with respect to k goes to zero (Bender & Orszag, 2013). At so-called points of stationary phase, we have

$$\frac{x}{t} = \left.\frac{d\sigma}{dk}\right|_{k_{\mathrm{s}}}, \tag{14}$$

where k_{s} is the stationary wave number. Thus, for any given x and t with x/t bounded and constant, the response as $t \to \infty$ may be approximated solely by contributions close to k_{s}. Since $\mathcal{U}(k)$ varies slowly in k, it may be replaced with $\mathcal{U}(k_{\mathrm{s}})$ (higher order contributions from a Taylor expansion of $\mathcal{U}$ about k_{s} scale with t^{-1} relative to the leading-order term: (Bender & Orszag, 2013)). Taking a second-order Taylor expansion of $\sigma(k)$ about k_{s} yields an approximate expression for the phase:

$$k\frac{x}{t} - \sigma(k) \approx k_{\mathrm{s}}\frac{x}{t} - \sigma(k_{\mathrm{s}}) - \frac{1}{2}\left.\frac{d^2\sigma}{dk^2}\right|_{k_{\mathrm{s}}}(k-k_{\mathrm{s}})^2. \tag{15}$$

Now the only k dependence resides in the quadratic term of Equation (15). The path of integration is deformed via Cauchy's integral theorem, such that the imaginary part of the phase remains constant close to k_{s} (Bender & Orszag, 2013; Gaster, 1968). The dominant contribution from k_{s} lends considerable freedom in altering the bounds of integration to construct an integral that may be evaluated analytically, leading to the asymptotic form

$$u_1(x,t) \sim \frac{\sqrt{2\pi}e^{-i\pi/4}\mathcal{U}(k_{\mathrm{s}})}{\left[(d^2\sigma/dk^2)|_{k_{\mathrm{s}}}t\right]^{1/2}}e^{i[k_{\mathrm{s}}x-\sigma(k_{\mathrm{s}})t]}. \tag{16}$$

This shows that the imaginary part of $\sigma(k_s)$ sets the exponential growth or decay of the wave along the chosen characteristic, demonstrating the importance of the stationary wave number. Equivalent expressions have been presented in previous work on the asymptotic behaviour of unstable waves (Gaster, 1968; Merkine & Shafranek, 1980, P84). A more general discussion of the asymptotic methods used here can be found in Bender and Orszag (2013).

When the stationary wave number k_s is chosen to be the most unstable wave number k_m, then by definition $d\sigma_i/dk|_{k_m} = 0$, so that Equation (14) reduces to

$$d\sigma_r/dk|_{k_m} = x/t, \tag{17}$$

where $\sigma_r = \Re(\sigma)$. This gives the familiar result that the peak of an unstable wavepacket lies along a characteristic that moves at the group velocity evaluated at k_m.

The behaviour of $\sigma(k)$ close to the most unstable wave number does not necessarily provide information about the behaviour at a fixed location in space. From Equation (14), the wave number that dominates the asymptotic response at $x = 0$ must be a saddle point of $\sigma(k)$ satisfying $d\sigma/dk = 0$, or equivalently a merge between two branches of $k(\sigma)$ (Briggs, 1964). Since the peak is advected with the group velocity of the most unstable wave number, the behaviour at a fixed point in space will be that of a spatially amplifying wave, and k_s will be complex in general. If $\sigma_i(k_s) > 0$ at the saddle point, then the disturbance will grow at every point in the domain, in which case the instability is called absolute. Conversely if $\sigma_i(k_s) < 0$ the instability is convective; the amplitude will eventually decay to zero for all x after the peak has passed (Briggs, 1964; Huerre & Monkewitz, 1985). Figure 2a,b shows how absolute and convective instability, respectively, would manifest in the growth of an initially localized disturbance.

In a zonally varying flow, the presence of absolute instability permits, under certain conditions, the development of so-called local instabilities (P84). For a uniform domain, the growth rate at the most unstable real wave number provides an upper bound for the absolute growth rate (Huerre & Monkewitz, 1990). Simply put, the tail of a wavepacket cannot have a larger amplitude than the peak. However, if zonal variations exist such that the peak can travel into a region with sufficiently reduced instability, then the absolute growth rate of the exponential tail may exceed the now reduced growth rate of the peak, and a localized maximum of the amplitude can occur (P84). Necessary conditions for the existence of a local mode are closely linked to the presence of absolute instability. In the absence of local instability, a periodic domain is required to create a global instability of the system where convectively unstable wavepackets can re-enter the domain (P84, Huerre & Monkewitz, 1990).

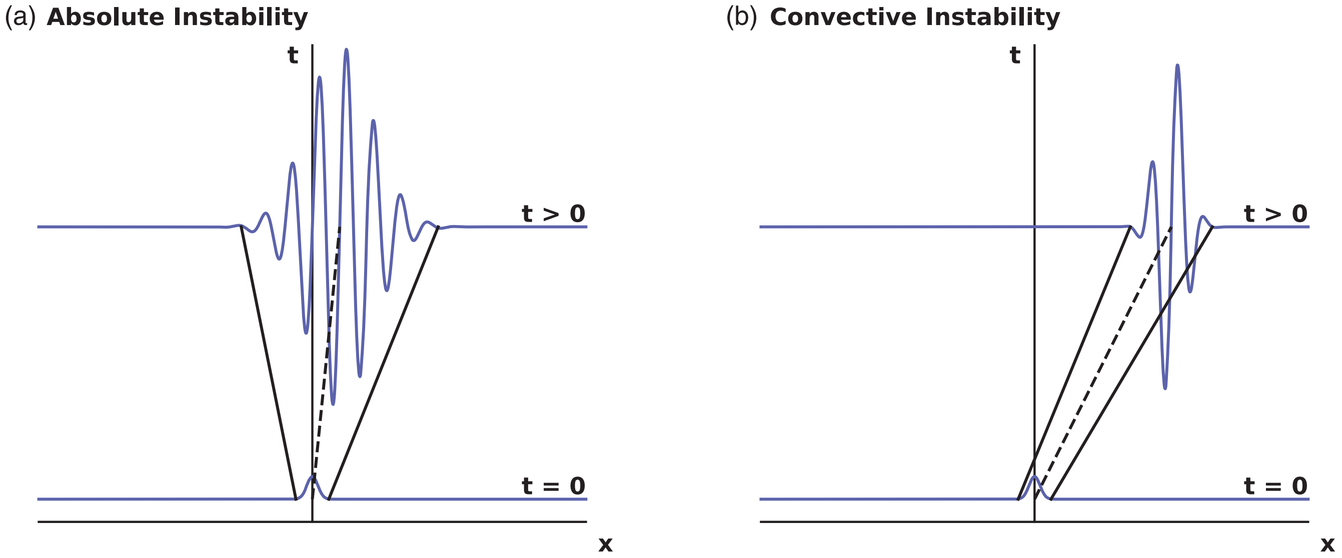

FIGURE 2 (a) Sketch of an absolutely unstable wave packet. Starting from a localized pulse disturbance at $t = 0$, the amplitude of the wave packet disperses in both directions. Any fixed point in space will have the amplitude of the wave packet grow in time. (b) Sketch of a convectively unstable wave packet. There exists some set of characteristics along which the amplitude grows in time, but for any fixed point in space the peak will eventually pass and the amplitude will decay. Based on a similar figure in Huerre and Monkewitz (1985).

3 | INSTABILITY OF MOISTURE-COUPLED WAVES

3.1 | Presence of absolute instability

We will first identify the nature of the spatial instabilities in the moist equatorial wave system by analysing the dispersion relation in the complex k-plane (Briggs, 1964; Merkine, 1977; Pierrehumbert, 1986). The procedure is drawn schematically in Figure 3. We evaluate $k(\sigma)$ for some chosen set of fixed values of σ_r, while decreasing σ_i from a positive value (which must be greater than the maximum growth rate for real k) to zero (Briggs, 1964). If the two branches of $k(\sigma)$ merge in the complex k-plane for $\sigma_i > 0$, with the branches originating separately from the upper and lower half-planes for large σ_i, then the system supports absolute instability (Briggs, 1964; Pierrehumbert, 1986). Otherwise, the branches merge for some negative value of σ_i and the instability is convective in nature. Since the dispersion relation for our system is quadratic in k, there can be only one saddle point.

The chosen set of rays in the complex σ-plane is shown in Figure 4a. The image of the σ-contours under the mapping $k(\sigma)$ for the Kelvin wave is shown in Figure 4b. Using the colour and thickness of the lines in Figure 4a as a guide, we can identify the two corresponding solutions of $k(\sigma)$ for any given σ. The information provided in the dispersion diagrams shown in Figure 1 is recovered whenever a contour of $k(\sigma)$ crosses the positive real line. It is clear that there is an absolute instability present, as the two branches merge close to the imaginary line (i.e., there exists a σ_s with $\Im(\sigma_s) > 0$ for which the two roots of the dispersion relation are equal). Since this merge happens at far greater length-scales than are realizable on Earth and is only weakly unstable, it does not appear to have much physical relevance. Figure 4c shows the image for the QE regime; here there exists a more compelling merge of the two branches. The branches of k originate separately from the upper and lower half-planes for large σ_i, confirming the physical relevance of this saddle point (Briggs, 1964; Pierrehumbert, 1986). The merge occurs at real wave number $ak_r \approx 0.75$ and linear frequency $\sigma_r/(2\pi) \approx 0.021\ \text{day}^{-1}$, so the absolute instability is realized at planetary scales and intraseasonal frequencies and has a phase speed of about $13\ \text{m}\cdot\text{s}^{-1}$, considerably slower than the phase speed evaluated at the most unstable wave number. The image for the WTG moisture-mode limit is shown in Figure 4d; since there is only one non-trivial branch, there is no possibility of a merge. However, it is clear that the lower branch of the QE regime resembles the dispersion relation for the WTG moisture mode when $\Re(k)$ becomes relatively large.

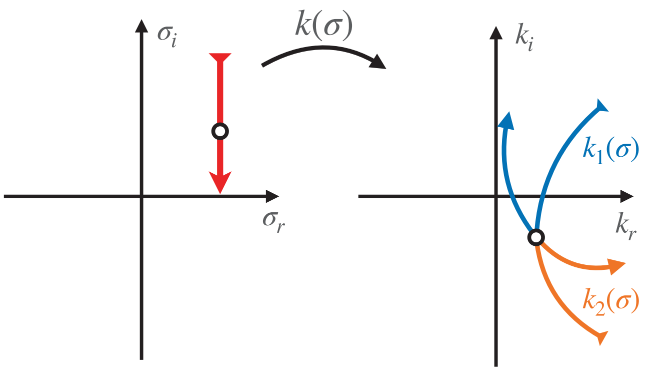

FIGURE 3 Schematic of the method for determining the nature of the spatial instability of the system. On the left, a ray in the complex σ-plane is drawn with constant real part, terminating at $\sigma_i = 0$. This ray is mapped into the complex k-plane using two different branches of the dispersion relation, as shown on the right. The point in the k-plane where the two branches merge (the open circle) defines the stationary wave number for $x/t = 0$. Since this merge occurs for a value of σ with $\sigma_i > 0$ and the two branches originate separately from the lower and upper half-planes, the system is absolutely unstable.

Given that we have separated out the meridional structure of the system, we must be circumspect that these solutions remain equatorially trapped when k as well as σ is complex. For the case of complex k, the meridional structure can be expressed in terms of $C = \sigma/k$ as

$$\mathcal{P}(y) = \exp\left(-\frac{\beta C_r y^2}{2|C|^2}\right)\exp\left(i\frac{\beta C_i y^2}{2|C|^2}\right), \tag{18}$$

where $C_r = \Re(C)$ and $C_i = \Im(C)$. Note that C_r is not the phase speed of a wave crest, which would instead be $\Re(\sigma)/\Re(k)$. The argument of the first exponential is purely real, while the argument of the second is purely imaginary. It is clear that the condition for equatorial trapping is $C_r > 0$. Figure 5 shows the real part of the phase speed evaluated on the contours in the k-plane presented above. The absolute instability of the QE mode is equatorially trapped. In the Kelvin-wave regime, the value of C_r at the absolute instability is close to zero, again calling the physical relevance of that saddle point into question.

Numerical integrations of the responses of the QE and Kelvin parameter regimes are shown in Figure 6a,b, respectively. It is clear that the QE wave packet grows in both directions, confirming the presence of absolute instability. The Kelvin-wave packet remains attached to $x = 0$, but does not show any significant growth there, alluding to its marginal absolute instability; that the wavelength of the Kelvin-wave packet grows towards $x = 0$ is also consistent with the theoretical prediction from the analysis of the dispersion relation, as the absolute instability occurs at

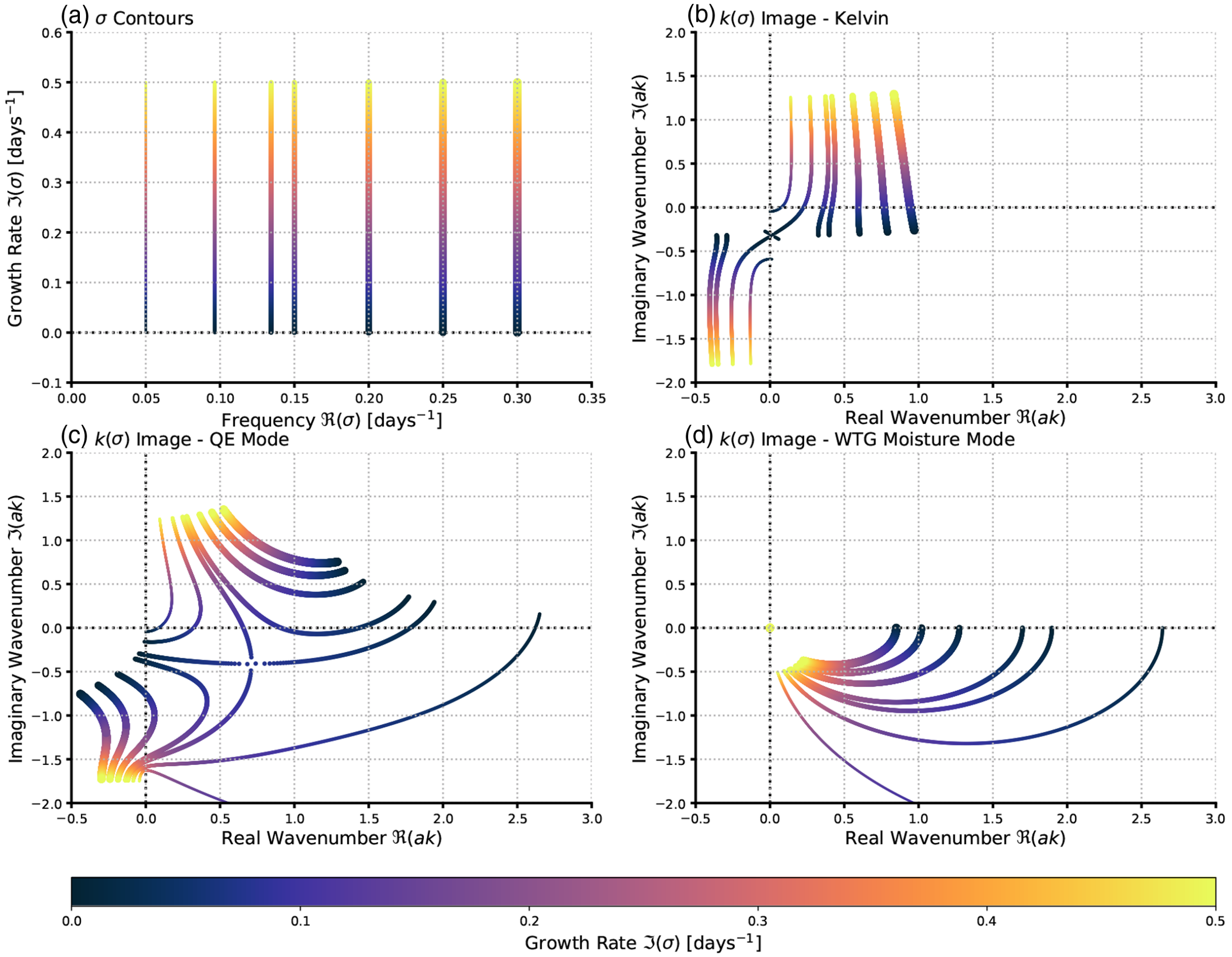

FIGURE 4 (a) Rays in the complex σ-plane. The shading indicates the imaginary part and the thickness of the line scales with the real part of σ. (b) The image of the σ-contours under the mapping $k(\sigma)$ in the complex k-plane for the Kelvin parameter regime. The mapping can be tracked by the thickness and shading of the lines in panel (a), which scale with the real and imaginary parts of σ, respectively. (c) As in (b) but for the QE regime. A clear merge between the two branches of $k(\sigma)$ is observed in the lower half-plane, where the dispersion curves form a cross pattern. (d) As in (b) but for the moisture-mode regime, in which only a single non-trivial branch exists.

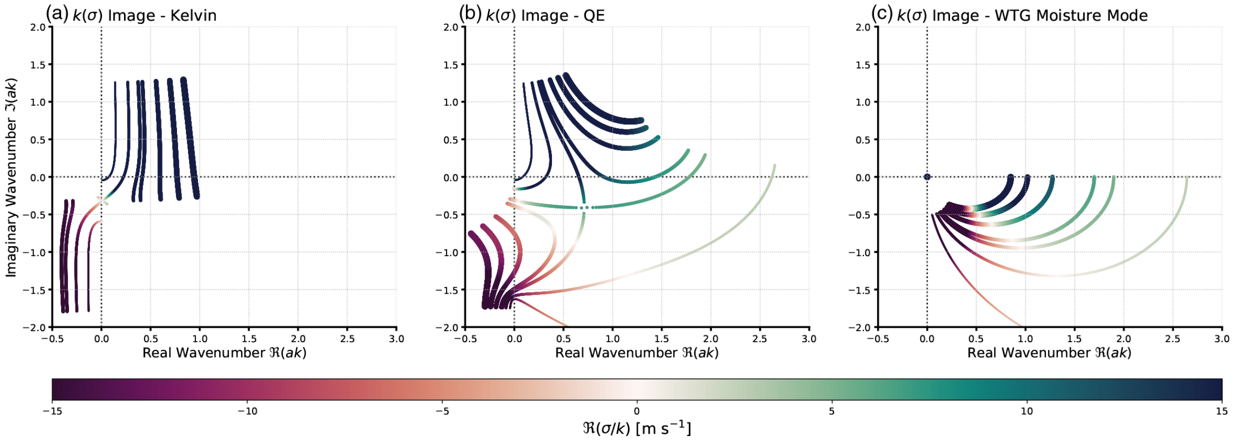

FIGURE 5 (a) Image of $k(\sigma)$ for the Kelvin regime coloured by the real part of σ/k. The σ contours are the same as those used in Figure 4. Negative values indicate solutions that are not equatorially trapped and diverge as $y \rightarrow \infty$, while positive values correspond to valid equatorially trapped waves. (b) As in (a) but for the QE regime. (c) As in (a) but for the WTG moisture-mode regime.

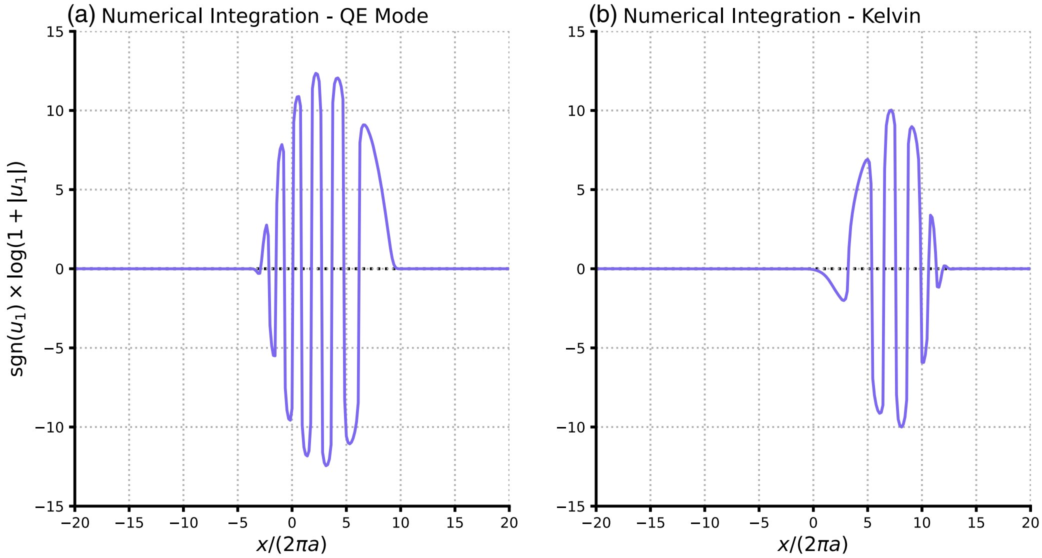

FIGURE 6 (a) Result of a long numerical integration ($\hat{t} = 500$) of the system in the QE regime, with $\tilde{M}_{\mathrm{e}} = 0$ and $\tau_{\mathrm{c}} = 12$ h. The solution is transformed as $\mathrm{sgn}(u_1)\log(1 + |u_1|)$ to show the behaviour near the tails of the wave packet better, while still retaining the fluctuations in the phase. (b) As in (a) but for the Kelvin-wave parameter regime of the system, with $\tilde{M}_{\mathrm{e}} = 0.2$ and $\tau_{\mathrm{c}} = 2$ h.

a much smaller wave number than the most unstable real wave number.

Figure 7 shows the amplitude growth over time in the numerical simulations, for both the translating peak of the disturbance and the stationary point $x = 0$. The amplitude at the peak is calculated as the maximum value of $|u_1|$ in the domain. Figure 7a shows these growth rates for the QE regime. It is clear that the theoretical predictions of the maximum growth rate and the absolute growth rate correctly characterize the amplitude at the peak of the wavepacket and at $x = 0$, respectively. Figure 7b shows the corresponding peak and absolute growth rates for the Kelvin regime of the system. Here the marginal absolute instability is clear; the amplitude at $x = 0$ shows a negligible tendency towards growth, as predicted from analysis of the dispersion relation. Additionally, the peak growth rate for the Kelvin wave is slightly less than that of the QE mode, as predicted from the dispersion diagrams shown in Figure 1b.

3.2 | Thermodynamics of asymptotic solutions

We are additionally interested in the degree to which the tendency of column-integrated moist enthalpy is set by perturbations to either temperature or moisture. In this simple linear system, the column-integrated moist enthalpy is given by

$$\langle h \rangle = -\frac{M_{\mathrm{s}}}{c^2}\phi_1 + \langle q \rangle. \qquad (19)$$

Following Ahmed *et al.* (2021), we use the ratio of moisture and temperature perturbations to understand which component controls the value of the moist enthalpy in each regime. For our linear model, the ratio is

$$\gamma \equiv -\frac{c^2\langle q \rangle}{M_{\mathrm{s}}\phi_1} = -i\frac{\tau_{\mathrm{c}}\sigma\left(1 + c^2k^2/\sigma^2\right)}{1 + r}. \qquad (20)$$

For waves with intraseasonal periods, we will have $|\tau_{\mathrm{c}}\sigma| \ll 1$, so the wave must be slow relative to the gravity-wave frequency ck in order for the moisture signal to dominate. Since γ will be complex in general, its modulus $|\gamma|$ will be used to measure the relative magnitude of moisture and temperature perturbations, while its argument $Arg(\gamma)$ describes the degree to which moisture and temperature perturbations are in phase. As noted previously, this also measures the phase between temperature and heating anomalies, since $\langle Q \rangle = (1 + r)\langle q \rangle / \tau_{\mathrm{c}}$.

Figure 8 displays $|\gamma|$ and $Arg(\gamma)$ evaluated on the dispersion curves in the complex k-plane from the previous section. Figure 8a–c shows $|\gamma|$ for each of the three parameter regimes. In the Kelvin limit, temperature anomalies dominate the moist enthalpy; over the whole range of frequencies we have $|\gamma| \ll 1$. In the QE regime, solutions transition from being more gravity-wave-like at large scales ($k \ll 1$) to more moisture-dominated at smaller scales ($k > 1$). At the saddle point itself, temperature and moisture contribute equally to the moist enthalpy. Finally, in the WTG moisture-mode limit $|\gamma| \gg 1$ and the thermodynamics is strongly controlled by moisture, as would be expected.

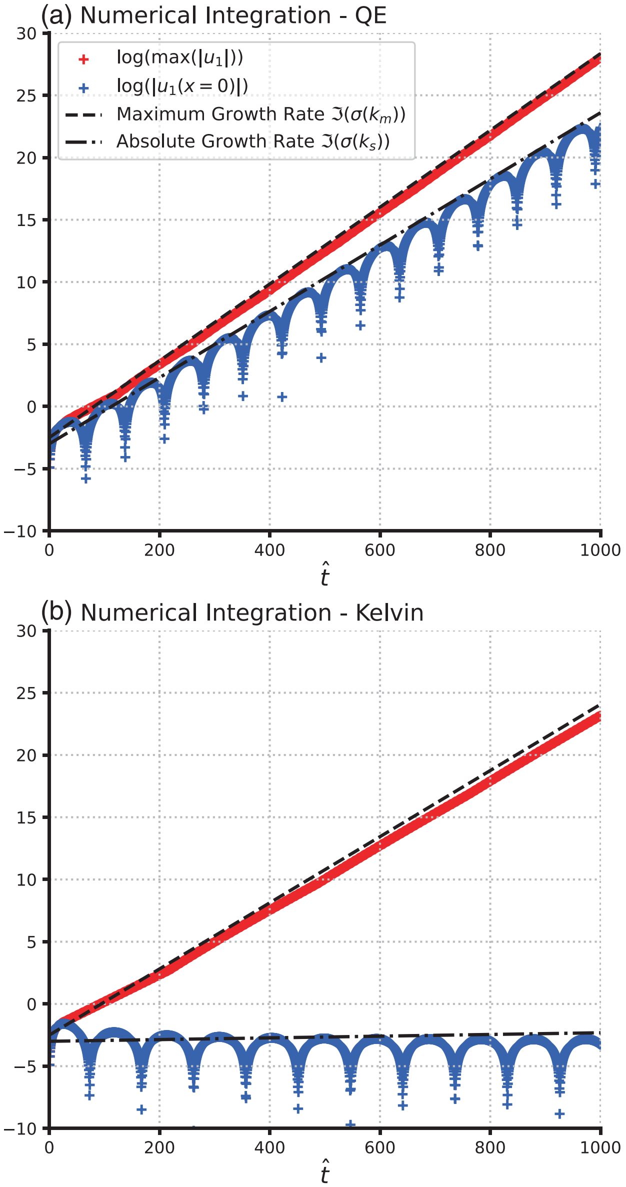

FIGURE 7 (a) Time series of amplitude growth in the QE regime. The crosses show the evolution of the logarithm of the maximum of $|u_1|$ achieved in the domain, and the value of the logarithm of $|u_1|$ at $x = 0$. The dashed line shows the theoretical prediction of the maximum growth rate, $\sigma_i(k_\mathrm{m})/\sqrt{\beta c}$, in the non-dimensional units of the numerical simulation. The dash–dotted line shows the predicted absolute growth rate $\sigma_i(k_s)/\sqrt{\beta c}$. (b) As in (a) but for the Kelvin-wave parameter regime of the system.

Figure 8d–f shows the same dispersion curves coloured by *Arg*(γ). Along the real line, all three regimes exhibit temperature and moisture anomalies that are roughly in quadrature, with temperature leading the moisture (and therefore the heating) as expected for a propagating deep-convective mode (Emanuel *et al.*, 1994). Indeed, *Arg*(γ) appears less dependent on the chosen parameter regime and more on the location in the k-plane. Waves that amplify in an eastward direction (those in the lower half-plane) generally have more in-phase perturbations, while those that are evanescent eastward have more out-of-phase relations between moisture and temperature. This is a simple consequence of the fact that an amplifying wave must have a source of variance generation; in this case the correlation between Q and T acts as that source. The essential convection–circulation interaction we have modelled puts a constraint on the governing thermodynamics of the system, such that amplifying waves are controlled more by moisture, while evanescent waves are controlled by temperature.

3.3 | Zonally varying basic states

Having confirmed the presence of absolute instability, we now investigate whether the system can support local modes of instability in a zonally varying flow. The Wentzel–Kramers–Brillouin (WKB) approximation will be used as a theoretical tool to investigate this issue. Direct association with the observed MJO is then challenging, because the MJO can be broadly thought of as a wave number 1 disturbance situated in a basic state that varies most strongly at similar length-scales. Strict application of the following theory is limited to infinite domains with basic-state variations occurring over much longer length-scales than the wavelength of the disturbance. Nevertheless, recent work has shown that local application of linear wave criteria can provide qualitative understanding of the zonal development and confinement of the MJO and other modes of tropical variability (Inoue *et al.*, 2021; Mayta & Adames, 2023; Mayta & Adames Corraliza, 2023).

The construction of the local mode closely follows the procedure of P84. We allow the parameters $(\tilde{M}_\mathrm{e}, \tau_\mathrm{c}, \tilde{A}_q)$ to vary in the zonal direction at $\mathcal{O}(1)$ in a slow coordinate $X = \epsilon x$, with $\epsilon \ll 1$. Note that no specific value is assigned to ϵ; it is tacitly assumed that there is *some* slow scale on which the WKB approximation will hold (P84). The eigenfunctions of the system have the form

$$u_1 = \mathcal{A}_u(X)e^{i\Theta(X)/\epsilon}e^{-i\sigma t}, \qquad (21)$$

where $\mathcal{A}_u(X)$ is the spatially varying amplitude of the wave, and $\Theta(X)$ sets the spatial amplification and phase of the wave. After adjusting Equation (6) suitably to allow the parameters $(\tilde{M}_\mathrm{e}, \tau_\mathrm{c}, \tilde{A}_q)$ to vary in the slow coordinate X, the dispersion relation for the system becomes, to leading order in the small parameter ϵ,

$$i\sigma^2 - c^2\Theta'^2\tau_\mathrm{c}\sigma - ic^2\Theta'^2(\tilde{M}_\mathrm{e} + i\tilde{A}_q\Theta'^{-1}) = 0, \qquad (22)$$

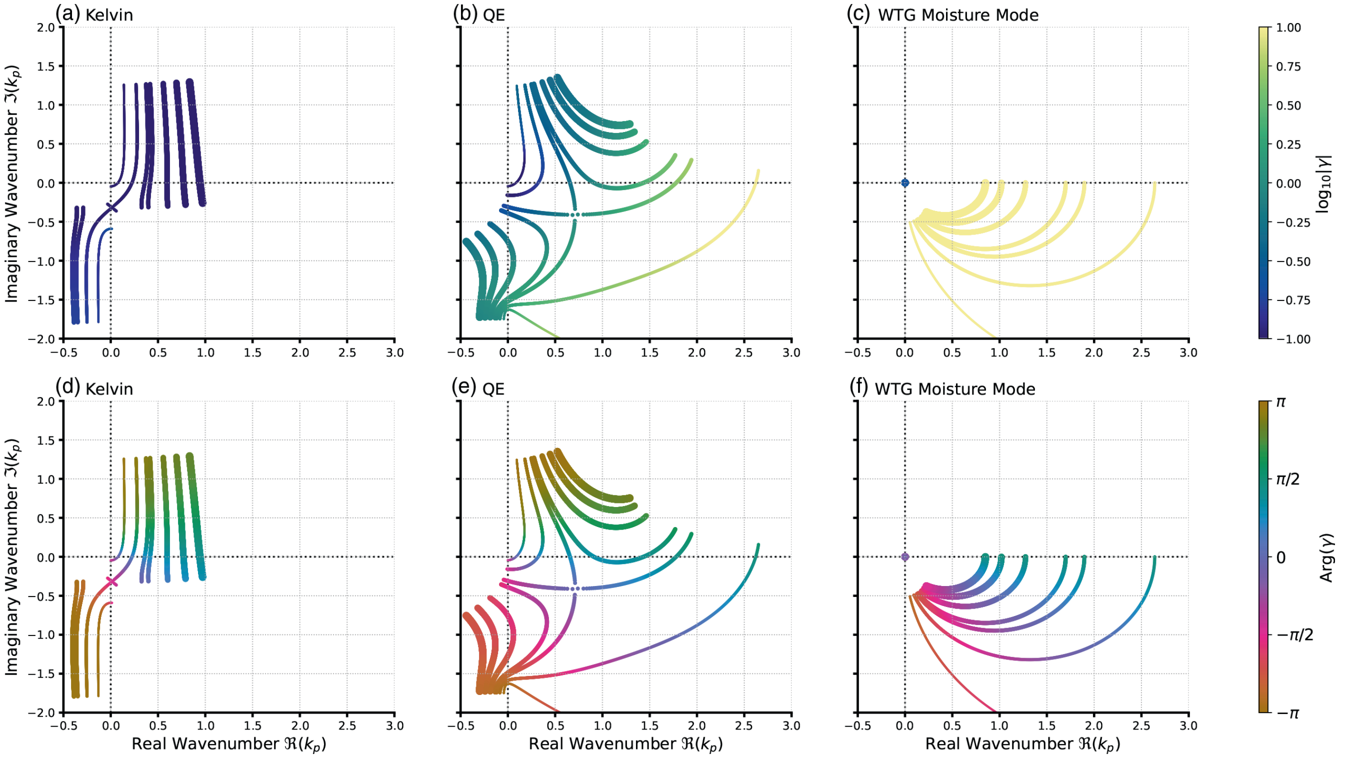

FIGURE 8 (a) Image of $k(\sigma)$ for the Kelvin regime, coloured by $|\gamma|$. Note the log scale for the colour bar. The σ contours are the same as those used in Figure 4. (b) As in (a), but for the QE mode. (c) As in (a), but for the WTG moisture-mode limit. (d) Image for the Kelvin regime coloured by $Arg(\gamma)$. A positive argument represents temperature anomalies leading moisture anomalies (to the east). (e) As in (d), but for the QE mode. (f) As in (d), but for the WTG moisture-mode limit.

where $\Theta' = d\Theta/dX$, $\tilde{M}_e$, and τ_c are all functions of the slow coordinate X, and as before we have dropped the term that is cubic in σ. This is simply the dispersion relation of the uniform system with the wave number k replaced by $\Theta'(X)$. An analysis of the meridional structure problem produces an expression for the slowly varying meridional shape of the solution that bears a similar resemblance to its counterpart in the uniform system.

We now consider the conditions for the existance of a local mode of instability. Values of the parameters $(\tilde{M}_e, \tau_c, \tilde{A}_q)$ are selected that produce an absolute instability with complex frequency σ_s; it is assumed that the system takes on these values at $X = 0$. We then calculate $k(\sigma_s; X)$, where k has now been conflated with $\Theta'(X)$ in Equation (22). The notation has been chosen to indicate that k depends on the slow coordinate X through the parameters $(\tilde{M}_e, \tau_c, \tilde{A}_q)$. The parameters must be chosen to vary in X in such a manner that the absolute growth rate—which may be calculated locally from the WKB dispersion relation for each X— decreases away from $X = 0$. Requiring that the absolute growth rate attains a local maximum where $(d\tilde{M}_e/dX) = 0$ and $(d\tau_c/dX) = 0$ is important to prevent the breakdown of WKB theory (P84). By construction, the value of $k(\sigma_s; X = 0)$ is the same for the two branches of k, so the solution will switch branches at this point. Should the sign of $k_i(\sigma_s; X)$ change for one of the branches of k as X is moved away from zero, then the solution switches the spatial direction in which it amplifies, and the constructed mode is a seamless continuation of amplifying and evanescent waves. The resulting instability is then localized in space (P84).

These theoretical requirements for the existence of local instability put constraints on the zonal structure of the parameters $(\tilde{M}_e, \tau_c, \tilde{A}_q)$; it is reasonable to ask whether the resulting basic state bears any resemblance to the observed Indo-Pacific WP. In general, a simple way to reduce the absolute growth rate of the system is simultaneously to increase $\tilde{M}_e$ and decrease τ_c. In other words, moving the system towards the Kelvin-wave regime will reduce the absolute growth rate. The WP, and specifically the Indian Ocean basin, are well-known to be associated with a local minimum of the effective GMS (Inoue *et al.*, 2021; Mayta & Adames Corraliza, 2023). Mayta and Adames Corraliza (2023) have also shown that the observed convective relaxation time-scale τ_c exhibits a local maximum over the Indian Ocean. In this sense, the observed WP is qualitatively consistent with the structure of a region of increased absolute growth rate, so we idealize the WP as a region with reduced $\tilde{M}_e$ and increased τ_c. Equivalently, as we move away from the centre of the

WP, the system moves towards the Kelvin-wave limit of the system.

Figure 9a shows how the real and imaginary parts of the wave number change as the basic-state parameters are moved together from the QE regime to the Kelvin limit. As intended, the two branches of $k(\sigma_{\mathrm{s}})$ merge at the assumed values of $\tilde{M}_{\mathrm{e}}$ and τ_{c} that produce the largest absolute growth rate. It is clear that the imaginary parts of the two branches take on different signs when the system has been moved sufficiently far from the point of maximum absolute growth rate. The solution is able to switch smoothly between amplifying and evanescent waves and hence local instability can be realized in the system. It is important to note that the system does not need to be moved far towards the Kelvin regime to produce a local mode. Sensitivity experiments with different choices of $\tilde{M}_{\mathrm{e}}$ and τ_{c} at $x = 0$ suggest that the minimum value of $\tilde{M}_{\mathrm{e}}$ in the domain must be less than zero in order for local instability to exist; we have chosen a strongly negative value of $\tilde{M}_{\mathrm{e}} = -0.1$ to illustrate the local instability clearly. Figure 9b shows how the wave number responds to a decreasing moistening parameter $\tilde{A}_q$. Again we see that the imaginary parts of the two branches take on opposite signs, and so a local instability is possible. However, given that this parameter is an aggregation of many disparate processes, the response shown in Figure 9a is likely more amenable to association with the observed WP.

Having confirmed the potential for local instability in the system, we now look at the zonal structure of such a mode. Figure 10 shows the behaviour for a simple zonally varying domain in which $\tilde{M}_{\mathrm{e}}$ and τ_{c} both take on Gaussian profiles in the zonal direction, of the form

$$\tilde{M}_{\mathrm{e}} = -0.07 - 0.03\exp[-\hat{x}^2/(2L_{\mathrm{w}}^2)], \tag{23a}$$

$$\tau_{\mathrm{c}} = 14 + 2\exp[-\hat{x}^2/(2L_{\mathrm{w}}^2)], \tag{23b}$$

where $\tilde{M}_{\mathrm{e}}$ is dimensionless and τ_{c} is given in units of hours, $\hat{x}$ is the dimensionless zonal coordinate introduced in Section 2.2, and L_{w} is a non-dimensional length-scale that controls the width of the region of increased instability. Using Figure 9 as a guide, the specific values of the parameters are chosen such that the imaginary parts of the two branches of $k(\sigma_{\mathrm{s}}; X)$ take on different signs as $x \to \infty$. Moving the system too far into the Kelvin regime when moving away from $x = 0$ can lead to solutions that are not equatorially trapped. For reference, the structures of $\tilde{M}_{\mathrm{e}}$ and τ_{c} are shown in Figure 10a,b, respectively. Even though the branch switch itself occurs at $x = 0$, since the imaginary part of the wave number is positive at the coalescence point, the wave will be evanescent at

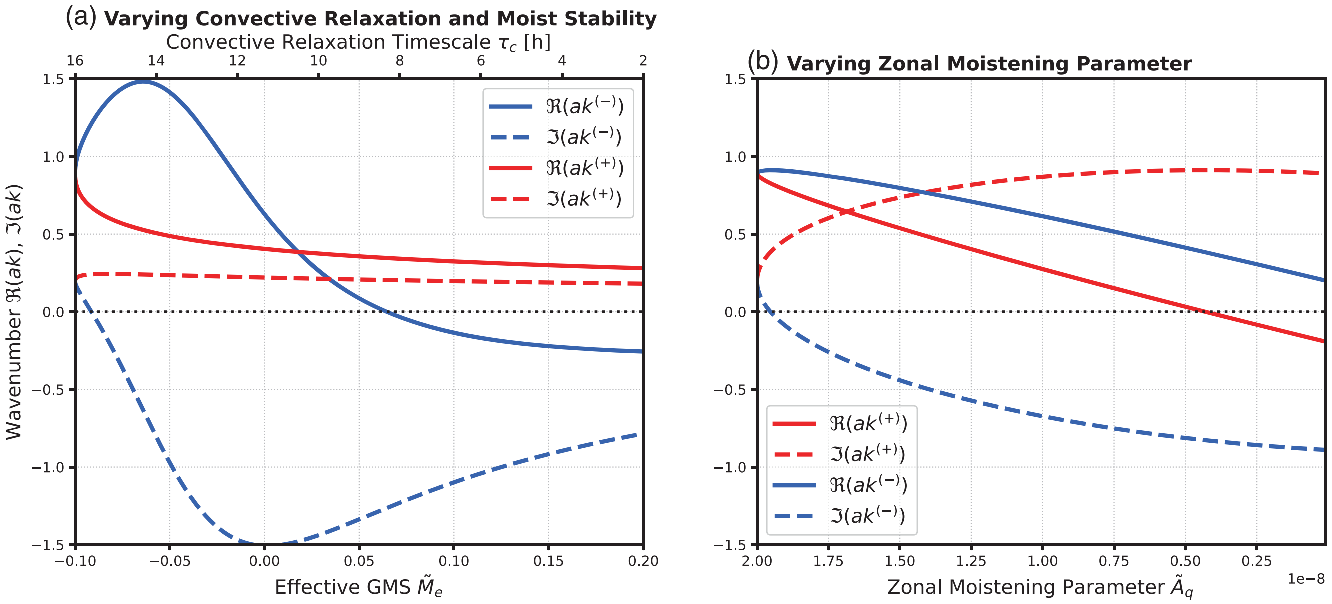

FIGURE 9 Analysis of the WKB dispersion relation for varying basic-state parameters. (a) The parameters $\tilde{M}_{\mathrm{e}}$ and τ_{c} are moved in unison from values in the QE regime to the Kelvin regime. The dispersion relation is solved for k as a function of $\tilde{M}_{\mathrm{e}}$ and τ_{c}, with σ fixed to the absolute frequency calculated for $\tilde{M}_{\mathrm{e}} = -0.1$ and $\tau_{\mathrm{c}} = 16$ h (the values the system is assumed to take on at $x = 0$). The resulting curves for the real and imaginary parts of the wave number are shown in solid and dashed curves, respectively. By construction, the two branches of k take on the same value when $\tilde{M}_{\mathrm{e}} = -0.1$ and $\tau_{\mathrm{c}} = 16$ h. Note that there are some points where the two imaginary parts take on different signs. (b) The zonal moistening parameter $\tilde{A}_q$ is decreased from a maximum value of 2×10^{-8} m to zero. Again the imaginary parts of the two roots take on different signs for sufficiently small values of $\tilde{A}_q$.

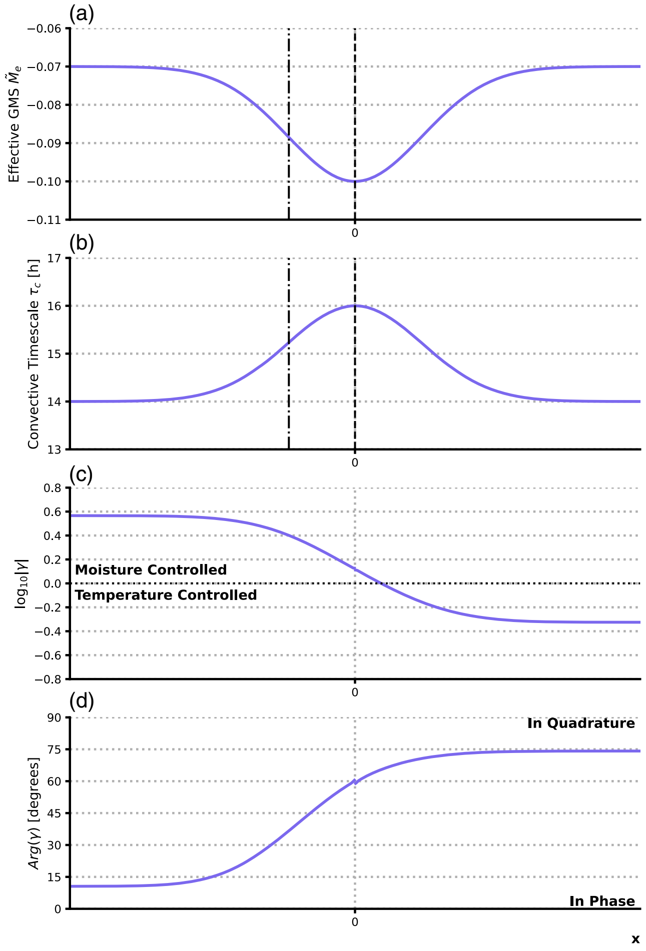

FIGURE 10 Structure of the simple zonally varying basic state and the zonal development of the resulting local mode. (a) Zonal structure of the effective GMS $\tilde{M}_{\mathrm{e}}$. The chosen scale for x is arbitrary. The black dashed line denotes the location at which the branch switch occurs ($x = 0$). The black dash–dotted line shows the point at which the solution switches from amplifying to evanescent. (b) As in (a), but for the convective time-scale τ_{c}. (c) Modulus of the resultant q–T ratio γ as a function of x as predicted by the local WKB analysis. (d) Argument of γ as a function of x for the local mode.

$x = 0$, and will achieve its maximum amplitude at some $x < 0$ (P84).

We will again use the q–T ratio γ to characterize the thermodynamic structure of the solutions. The response of the modulus and argument of γ as a function of x are shown in Figure 10c,d, respectively. For $x < 0$, the thermodynamics of the mode are is controlled more by moisture, and the temperature and moisture anomalies of the mode are close to being in phase. Moving eastward through the domain, temperature and moisture perturbations transition to being more out of phase, and the moist enthalpy becomes progressively more controlled by temperature. The importance of this asymmetric response should be highlighted; a simpler WKB analysis of the dispersion relation for real k in a zonally varying domain would not be able to describe this development. The concepts of absolute instability and branch switching play essential roles in producing the very different responses on either side of our idealized WP.

The theoretical predictions derived above can be checked via numerical simulation. Figure 11 shows snapshots of $\langle q \rangle$ and $\langle T \rangle$ in two different domains where $\tilde{M}_{\mathrm{e}}$ and τ_{c} take on the forms given in Equations (23a) and (23b): one with L_{w} large relative to the wavelength of the local mode (Figure 11a), and one where L_{w} is of the same order as the wavelength (Figure 11b). Moving eastward through the domain, temperature becomes progressively larger in magnitude relative to moisture, and the fields transition from being essentially in phase to in quadrature within the interval $[-5, 5]$. Thus the two qualitative predictions of the WKB analysis hold true in the numerical simulations. Indeed, even when the variation in the basic state is confined to a relatively short region (Figure 11b), these same zonal variations are observed in the system. The main alteration when imposing a narrow region of increased instability is that the envelope of the wave becomes more asymmetric about $x = 0$, in particular for the column water vapour $\langle q \rangle$ (Figure 11b).

Another assumption built into the WKB analysis of the local mode is that every point in the domain grows with the absolute growth rate evaluated at $x = 0$. Figure 12 shows the evolution of the amplitude at three different locations in the domain. It is clear that, after an initial adjustment period, all three locations take on essentially the same exponential growth rate, which matches well with the predicted absolute growth rate evaluated at $x = 0$. It is important to note that we have not enforced the local mode dynamics in these numerical experiments; in stepping the system forward in time, we observe behaviour that greatly resembles the predictions made by the WKB analysis.

4 | ADDITIONAL LINEAR MODELS

4.1 | Inclusion of momentum damping

The model studied in Section 3.1 is free from any damping in the momentum equation, following previous works on the linear modes of the tropical atmosphere (Adames *et al.*, 2019; Ahmed *et al.*, 2021). However, momentum damping has elsewhere been put forth as an essential component to the dynamics of the MJO (Kim & Zhang, 2021). Zonal momentum budgets calculated from reanalysis data suggest that advective tendencies can contribute to a strong effective linear damping rate for the MJO, with a

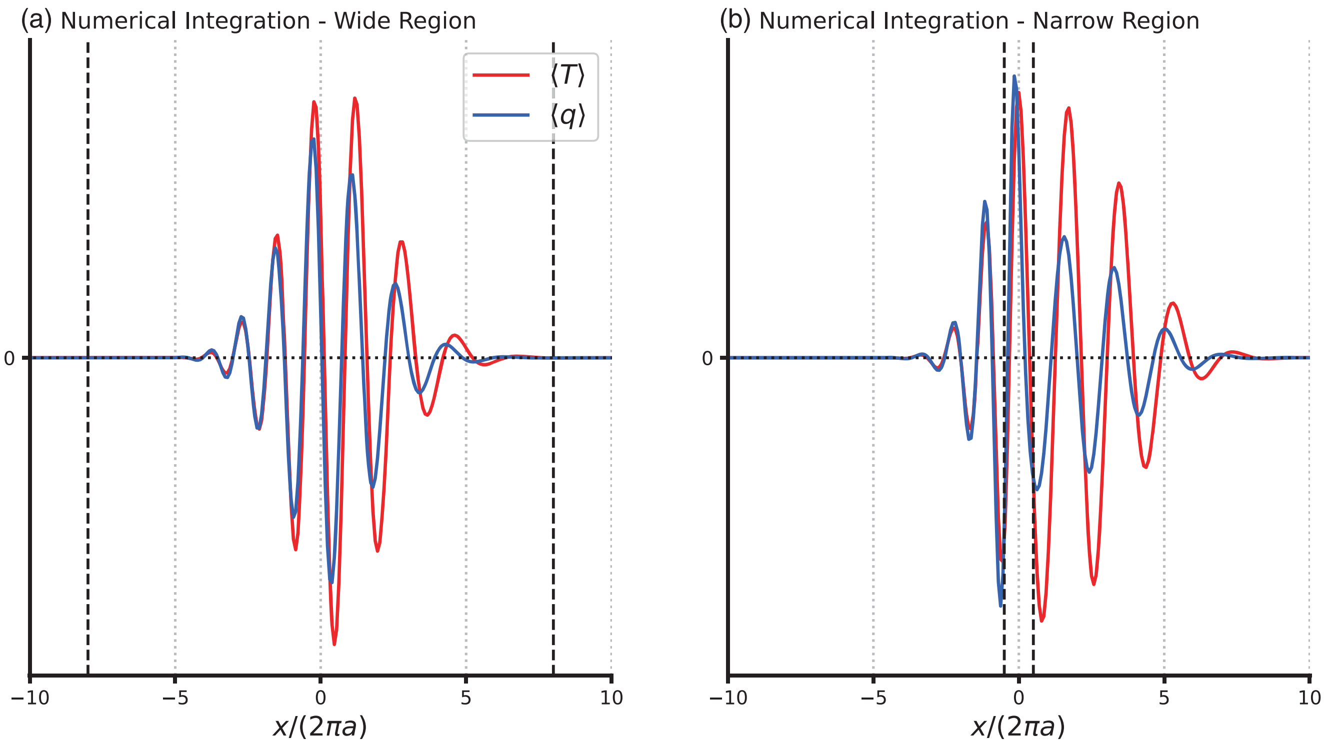

FIGURE 11 (a) Snapshot of the numerical simulation at $\hat{t} = 1000$ for a zonally varying basic state with $L_{\mathrm{w}} = 4$. The plotted fields are the column-integrated temperature perturbation $\langle T\rangle = -M_{\mathrm{s}}\phi_1/c^2$ and the column-integrated water vapour $\langle q\rangle$. The vertical dashed lines are located at $\pm 2L_{\mathrm{w}}$. (b) As in (a) but for a simulation with a much narrower region of zonal variations, with $L_{\mathrm{w}} = 0.25$.

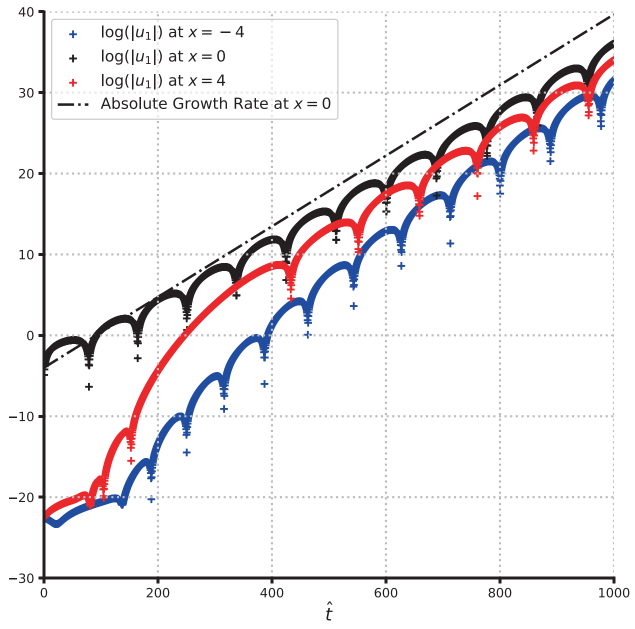

FIGURE 12 Amplitude growth in time at three different points in the zonally varying simulation with a wide region of increased instability. The crosses denote the logarithm of $|u_1|$ at $x = -4$, $x = 0$, and $x = 4$. The dash–dotted line shows the predicted absolute growth rate at $x = 0$.

time-scale of 3–5 days (Lin *et al.*, 2005). This large damping rate is necessarily empirical, but is the most straightforward way to account for additional unwieldy terms in the zonal momentum budget. With the inclusion of momentum damping, the zonal momentum equation can be rewritten as

$$\frac{\partial u_1}{\partial t} + \frac{\partial \phi_1}{\partial x} = -\epsilon_u u_1, \tag{24}$$

where ϵ_u is a linear damping coefficient that takes on the value of (3.5 days)$^{-1}$ suggested by Kim and Zhang (2021). The new dispersion relation for the damped system is given by

$$i\sigma^2 - \left(c^2k^2\tau_{\mathrm{c}} + \epsilon_u\right)\sigma - ic^2k^2\left(\tilde{M}_{\mathrm{e}} + i\tilde{A}_q k^{-1}\right) = 0, \tag{25}$$

so the system is again quadratic in both σ and k.

For real k, this modification of the dispersion relation reduces the maximum growth rate of the QE regime, and slows the phase speed slightly (not shown). Figure 13 shows contours of σ mapped into the complex k-plane under the dispersion relation for the damped system, similar to the mappings shown in Figure 4 for the undamped system. A merge of the two branches is still evident for the damped system. This merge again appears at intraseasonal

(a) σ Contours

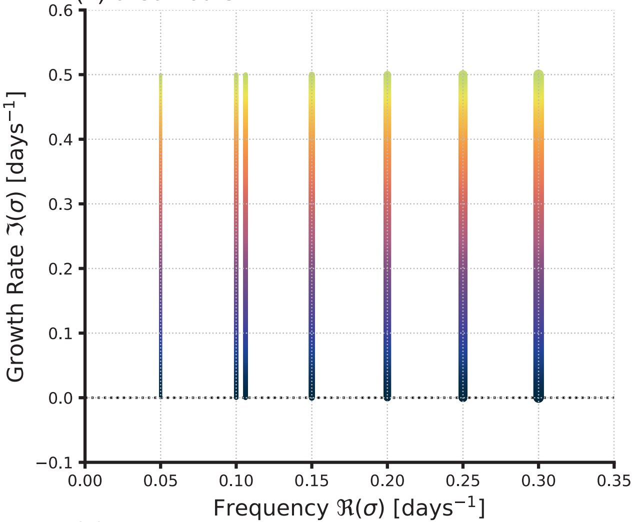

(b) $k(\sigma)$ Image - QE Damped

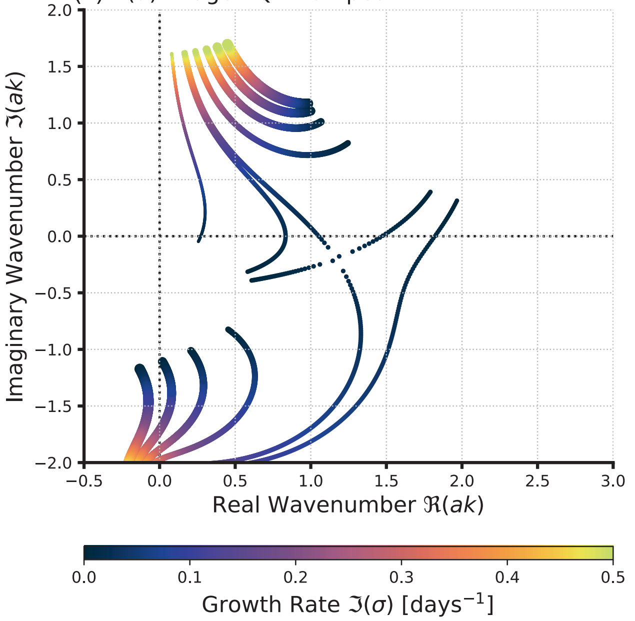

FIGURE 13 (a) Contours in the σ-plane, which will be mapped into the k-plane using the damped dispersion relation. (b) Corresponding contours of $k(\sigma)$ in the complex k-plane for the damped system. A merge between the two branches is located near the real line at $\Re(ak) \approx 1.2$, indicating the presence of absolute instability.

time-scales, though the absolute growth rate is reduced significantly relative to the undamped system. The fact that absolute instability is still supported with this much reduced growth rate lends us confidence that absolute instability is a quite robust feature of the system when $\tilde{M}_e$ is sufficiently small and τ_c sufficiently large. Note also that the addition of momentum damping has reduced the phase speed evaluated at the absolute instability to around $7\,\mathrm{m{\cdot}s^{-1}}$, closer to the observed propagation speed of the MJO.

4.2 | Inclusion of meridional winds

The $v = 0$ model we have developed in Section 2.1 illustrates the presence of absolute instability in low-frequency convectively coupled equatorial waves. However, systems with a non-zero meridional wind—and the accompanying meridional moisture advection—provide more compelling models of the MJO (Ahmed, 2021; Emanuel, 2020; Wang & Sobel, 2022a). To assess the relevance of absolute instability to the MJO better, we now analyse such a system. In the Appendix, it is shown that Equations (4a)–(4d) can be reduced to a single ordinary differential equation for the meridional structure of the meridional wind, which takes the form

$$\frac{d^2v_1}{dy^2} + D_0 y\frac{dv_1}{dy} + (D_1 + D_2y^2)v_1 = 0, \qquad (26)$$

where the coefficients of the equation are functions of σ and k that are given by

$$D_0 = \frac{i\beta\tilde{A}_q/\sigma - \tilde{B}_q}{i\sigma\tau_c - \tilde{M}_e}, \qquad (27a)$$

$$D_1 = D_0 - \frac{k\beta}{\sigma} - k^2 - \frac{\sigma^2(1 - i\sigma\tau_c)/c^2 - i\tilde{A}_q k}{i\sigma\tau_c - \tilde{M}_e}, \qquad (27b)$$

$$D_2 = \frac{\beta^2(1 - i\sigma\tau_c)/c^2 - \beta k\tilde{B}_q/\sigma}{i\sigma\tau_c - \tilde{M}_e}, \qquad (27c)$$

where $\tilde{B}_q = (1 + r)B_q/M_s$ is a rescaled meridional moisture advection parameter. The associated dispersion relation for any positive integer n is derived in the Appendix and is given by

$$D_1^2 - D_1D_0 + \frac{1}{4}D_0^2 - (2n + 1)^2\left(\frac{1}{4}D_0^2 - D_2\right) = 0. \qquad (28)$$

We focus solely on the $n = 1$ dispersion relation, though higher order and antisymmetric solutions have been presented by Wang *et al.* (2022). The dispersion relation is eighth order in σ, and fourth order in k. Despite the higher order of the equation, the absolute instability analysis proceeds in much the same manner as in Section 3.1, by mapping values of σ into the complex k-plane using the dispersion relation. Indeed, for intraseasonal frequencies, only two branches of $k(\sigma)$ yield wave numbers on the planetary scale. There is also an accompanying condition for the equatorial trapping of the solutions, which takes the form

$$\Re\left(\frac{D_0}{2} + \left(\frac{D_0^2}{4} - D_2\right)^{1/2}\right) > 0; \qquad (29)$$

Ahmed *et al.* (2021) derived an essentially identical trapping condition for their model.

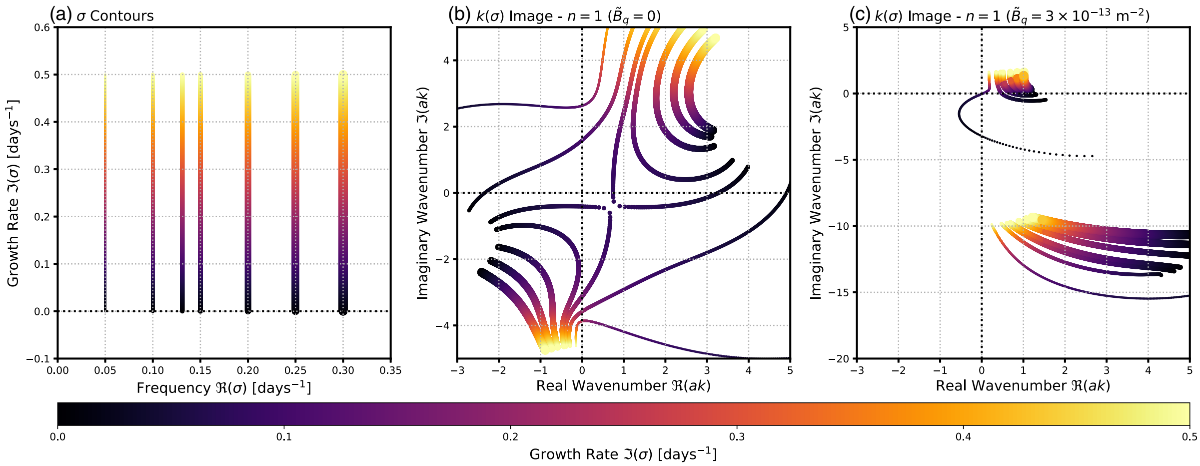

FIGURE 14 (a) Contours in the σ-plane, which will be mapped in the k-plane using the $n = 1$ dispersion relation. (b) Corresponding contours of $k(\sigma)$ in the complex k-plane for the $n = 1$ system with no meridional moisture gradient ($\tilde{B}_q = 0$). (c) As in panel (b) but for the $n = 1$ system with a non-zero meridional moisture gradient ($\tilde{B}_q = 3 \times 10^{-13}$ m^{-2}). Note the different axis limits in panels (b) and (c).

The resulting dispersion curves in the complex k-plane are shown in Figure 14; as before, the chosen contours in the σ-plane are displayed in Figure 14a. In Figure 14b the dispersion curves shown for a system with no meridional moisture gradient, that is, $\tilde{B}_q = 0$. There is evidently an absolute instability near the real line at $\mathfrak{R}(ak) \approx 0.75$, essentially the same position as was found for the $v = 0$ system. It has been confirmed using Equation (29) that this absolute instability is equatorially trapped (not shown). Interestingly, when we include a non-zero meridional moisture gradient into the system (we have set $\tilde{B}_q = 3 \times 10^{-13}$ m^{-2}, consistent with Ahmed *et al.* (2021)), we find that there is no longer an absolute instability present. This is illustrated by the dispersion curves in Figure 14c, where no branch merge is present. Further discussion of this result is provided in Section 5.2.

Figure 15 shows the accompanying WKB analysis of the $n = 1$ dispersion relation for the case with $\tilde{B}_q = 0$. As in the $v = 0$ case, the imaginary parts of the two relevant roots take on different signs as the system is moved towards the Kelvin limit, so local instability is possible. The interpretation is made somewhat more difficult since the real part of one of the roots changes sign for even a small increase in $\tilde{M}_\mathrm{e}$, but this is likely sensitive to the specific parameter choices we have made.

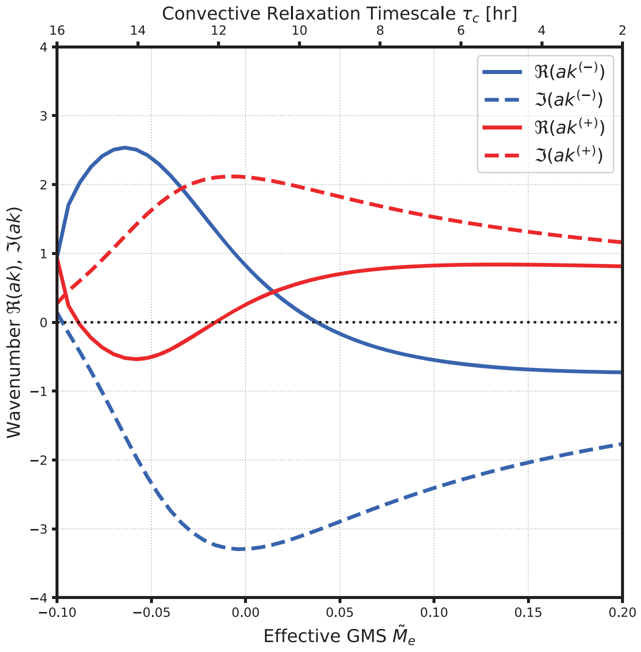

FIGURE 15 As in Figure 9, but for the $n = 1$ dispersion relation with no meridional moisture gradient ($\tilde{B}_q = 0$).

5 | DISCUSSION

5.1 | Implications for intraseasonal variability

The analysis presented above has shown that a simple linear model of tropical dynamics responds asymmetrically across a symmetric region of increased instability. Numerical simulations of this development matched quite well with theoretical predictions provided by a WKB analysis of the system, guided by the underlying knowledge that the relevant unstable solutions are in fact absolutely unstable. The theoretical conditions for the existence of a local instability imposed a zonal structure that was qualitatively consistent with the observed zonal variations of the WP (Inoue *et al.*, 2021; Mayta & Adames Corraliza, 2023). In other words, it seems reasonable that the WP is associated with a maximum of the absolute growth rate of our linear system. In our idealized domain, the resulting asymmetry of the wave solution was such that heating and temperature perturbations were more in phase for $x < 0$ and more in quadrature for $x > 0$. Together with these phase variations, the column-integrated moist enthalpy transitioned from being controlled more by moisture perturbations for $x < 0$ to being controlled more by temperature perturbations for $x > 0$. These results were confirmed numerically, and it was found that the predictions extended quite well to basic states with zonal variations which varied on length-scales of the same order as the wavelength of the instability (see Figure 11). The resulting zonal structure of the local instability is compelling because it shares some basic characteristics with the zonal development of the observed MJO. In particular, the transition of the phase between moisture—and therefore heating—and temperature is reminiscent of the transition seen in the observed MJO (Hendon & Salby, 1994). The gradual change in the relative magnitudes of moisture and temperature perturbations also bears some potential similarity to the zonal development of the MJO (Mayta & Adames, 2023). The smoothness of the gravity-wave transition on the eastern flank of the domain is qualitatively consistent with the analysis of Roundy (2012a, 2012b). While this connection is compelling, it must be tempered by the fact that in our linear model the transition occurs over numerous wavelengths of the disturbance, whereas in the actual MJO this development occurs within a much shorter region.

Viewing the MJO through the lens of absolute instability has important implications for the initiation of the MJO, in particular for "successive" MJO events, which are directly preceded by a previous cycle of the oscillation (Matthews, 2008). Powell and Houze Jr (2015) suggested that initiation of successive MJO events is achieved through the circumnavigation of a fast-moving, dry Kelvin wave originating from the previous cycle of the MJO. However, several modelling results that explicitly removed this pathway for initiation still produced successive MJO events (Maloney & Wolding, 2015; Ray & Li, 2013; Zhao *et al.*, 2013). Circumnavigating disturbances could still interfere constructively with the initiating phase of the MJO to promote growth (Maloney & Wolding, 2015), but these modelling studies suggest that the excitation of an MJO event can be caused by the previous event through processes local to the WP. Heuristically, such an initiation mechanism seems consistent with the notion of absolute instability—the presence of a disturbance at some longitude implies the maintenance of the wave amplitude at that position for future times.

The presence or absence of absolute instability is also intricately linked to the group velocity of an unstable wave. The presence of absolute instability allows energy to disperse in a direction opposite to the group velocity as evaluated at the most unstable wave number. This point is illustrated by Figure 6a: while the displacement of the peak is obviously eastward, the absolute instability causes wave energy to be dispersed westward as well as eastward. There has been much discussion as to whether the MJO has a westward group velocity, with some observational studies affirming this viewpoint (Adames & Kim, 2016) and others arguing that the group velocity is approximately zero (Chen & Wang, 2018). More recent syntheses of observations have pointed to a diverse range of dispersive behaviours for the MJO (Wei *et al.*, 2023), encompassing both of these previous pictures. Such conclusions are made by tracking the position of successive maxima and minima in precipitation or outgoing longwave radiation through individual or composite MJO events (Adames & Kim, 2016). In this sense, these studies measure the group velocity evaluated at the most unstable wave number. From the viewpoint of absolute instability, the more important question is whether the group velocity changes sign within the envelope of the MJO. Thinking of the MJO as an absolutely unstable wave may provide a new perspective from which to analyse the observed dispersion of the MJO.

5.2 | Caveats

There are a number of caveats to the analysis that we have presented here. Foremost among these concerns is our use of a linear, analytic model to represent the tropical atmosphere and its wave variability. While this choice is made so that we can appeal to the mathematical results provided by Briggs (1964) and P84, in doing so we have neglected much of the complexity of the real MJO. Perhaps most notably, precipitation is by definition a positive semi-definite quantity. In our linear framework we have implicitly described precipitation as a perturbation upon a precipitating mean state; in general, the linearly unstable solution will eventually reach an amplitude exceeding this mean state value and the model becomes physically unreasonable. We have intentionally run our numerical simulations for long times to allow the asymptotic behaviour to dominate, ignoring this deficiency of the linear framework. In reality, there must be some nonlinear process that curtails the linear growth of the wave solutions. Without a strong understanding of this occlusion process, the actual relevance of the asymptotic limit of the linear system remains uncertain.

Even accepting the necessity of a linear framework to acquire analytical results for unstable waves, our choice of model is not definitive. Each study of the linear modes of tropical variability has its own interpretation of the physical processes needed to represent low-frequency variability (Fuchs-Stone & Emanuel, 2022; Jiang *et al.*, 2020; Zhang *et al.*, 2020). There is considerable uncertainty in the interpretation of the moistening process $\tilde{A}_q$. In our interpretation, this parameter is a conglomeration of various terms in the moisture equation, some of which cannot be easily fitted into the first baroclinic mode paradigm with which we work (Adames *et al.*, 2019; Sobel & Maloney, 2013). Analysis of the moisture budget in models or reanalyses can aid in interpretation (MacDonald & Ming, 2022; Maloney, 2009), but forming a robust connection between the moisture budget and a single linear feedback on the zonal wind will always be challenging. Furthermore, we have represented the effective reduction of the GMS through cloud–radiation feedback, but modelling results suggest that such a strong feedback may not be necessary to produce MJO variability in the presence of zonal asymmetry (MacDonald & Ming, 2022). This indicates that the parameter $\tilde{M}_e$ may also need to be viewed more generally.

The presence of absolute instability was confirmed in models both with and without a meridional wind field, however it was found that the introduction of a term related to meridional moisture advection removed the absolute instability from the system. At the moment, it is unclear why the inclusion of this term should affect the spatial instability of the linear model so strongly, though it can be seen from Figure 14c that the introduction of this term drastically changes the structure of the dispersion relation in the lower half k-plane. It is important to note that the addition of this term does not appear to be singular, that is, the absolute instability is restored when the magnitude of $\tilde{B}_q$ is reduced by a factor of 3 to a value of 1×10^{-13} m^{-2} (not shown). Further examination of the dispersion relation has suggested that $\tilde{B}_q$ exerts its influence primarily through its modification of the D_2 coefficient in Equation (26)—a quick scale analysis suggests that, for $\tilde{B}_q$ of the order of 10^{-13} m^{-2} or greater, the contribution from $\tilde{B}_q$ is large relative to the term that scales with β^2/c^2. It may also be that the non-normality of the meridional basis functions, documented by Wang *et al.* (2022), will need to be taken into greater consideration to understand the complications brought on by non-zero $\tilde{B}_q$. These results serve to highlight some of the subtle differences between contemporary theories of the MJO. Wang and Sobel (2022a) motivate this term by showing that its inclusion leads to eigenmodes with horizontal structures that bear more resemblance to the observed MJO. Without this term included, our model is likely more similar to those of Fuchs and Raymond (2017) and Emanuel (2020) (see also Fuchs-Stone and Emanuel (2022)). It is worth noting that the meridional advection term included in the model is unphysical in a particular sense; in order for the meridional structure problem (Equation 26) to be analytically tractable, the background moisture field must be parabolic, and thus, for positive $\tilde{B}_q$, diverges to negative infinity in the limit $y \to \infty$. Wang and Sobel (2022a) point out that, because the solutions for v_1 decay exponentially, the overall meridional advection term will still decay as $y \to \infty$. Potential future work could look for numerical solutions to the meridional structure problem with a more general set of background moisture gradients to characterize better the role this term is playing in setting the temporal and spatial instability of the system.

6 | CONCLUSIONS

The scale selection and instability of the MJO are often explained via the derivation of linear models that produce the most unstable real wave number at planetary scales and intraseasonal frequencies (Adames & Kim, 2016; Ahmed, 2021; Fuchs & Raymond, 2017; Wang & Sobel, 2022a). We have instead investigated the asymptotic behaviour of localized pulses, effectively moving away from the normal mode picture that has been focused on in past work. The basis for this analysis is rooted in the theory of absolute and convective instability laid out by Briggs (1964). Using methods described by Briggs (1964) and Pierrehumbert (1986), it was found that simple linear models of the MJO have the property of absolute instability, so that wave amplitude will grow in a stationary frame of reference. This absolute instability was realized at planetary scales and intraseasonal frequencies, suggesting a potential connection to the MJO. The degree to which the waves were absolutely unstable was shown to be sensitive to certain model parameters. Absolute instability was found to be robust for what we referred to as the quasi-equilibrium (QE) mode, while regimes that produce unstable Kelvin waves were instead only marginally absolutely unstable. Numerical simulations of the model confirmed the predictions made based on the dispersion relation of the system. These results were derived using a model with no meridional wind, but it was found that they generalized quite well to a model with non-zero meridional wind, provided that only weak meridional moisture advection was included. With the inclusion of a sufficiently strong linear meridional moisture gradient, the instability became convective in nature.

The absolute instability of the QE mode was then leveraged to study these linear wave models in a zonally varying flow. Pierrehumbert (1984) stressed that it is in non-uniform systems that the implications of absolute instability become most important. We showed that zonal variations that mimic—in an idealized sense—an isolated warm pool can support localized modes of instability through the branch switching inherent to absolute instabilities. A WKB analysis of the system predicted an asymmetric response across the warm pool. The western flank of the warm pool ($x < 0$) was characterized by temperature and moisture perturbations being in phase, with moisture having a larger magnitude. The eastern part ($x > 0$), on the other hand, featured a quadrature relation between temperature and moisture, with temperature now being greater in magnitude. These predictions were borne out in numerical simulations, which showed strong agreement with the theoretical picture, even when the background state varied over relatively short length-scales.

The proposed significance of these results is that the zonal development of this simple linear model shows some similarity to the development of the MJO in its passage across the Indo-Pacific warm pool. We can then think of the essential convection–circulation coupling that gives rise to the temporal instability of the MJO as putting constraints on the structures of amplifying and evanescent waves. In this sense, our analysis says that low-frequency amplifying waves must have their moist enthalpy more controlled by moisture and evanescent waves must be controlled more by temperature. More work is needed to gain a more physically intuitive picture of why this should be the case. The fact that even this simple model of the MJO can predict this development lends some additional confidence that it captures some of the essential dynamics of the MJO, and furthers its role as a useful theoretical tool.

Further work is needed to understand the implications of absolute instability on tropical dynamics fully. In particular, uncertainties related to the occlusion of linear growth by nonlinear processes mean that conclusions based on the asymptotic behaviour of the system must be viewed with caution. While we have focused on connections to the MJO, these ideas may provide insights into the Boreal Summer Intraseasonal Oscillation, which can be modelled in a similar linear framework (Wang & Sobel, 2022a). Further extension of these concepts to the off-Equator moisture waves of Sobel *et al.* (2001) and Adames and Ming (2018) would be an interesting venture. This initial investigation provides evidence for the relevance of absolute instability to our understanding of the MJO and convectively coupled equatorial waves. In doing so, it provides a new perspective on tropical dynamics and demonstrates the critical role of zonal asymmetry in setting the behaviour of equatorial waves.

ACKNOWLEDGEMENTS

I thank Isaac Held for introducing me to the concepts of absolute and convective instability, and for helpful comments during the writing of this article. Further comments from Yi Ming and Wanying Kang were much appreciated. Finally, I thank two anonymous reviewers for their suggestions. This research was supported by the Co-operative Institute for Modeling the Earth System (CIMES) at Princeton University and NOAA GFDL.

FUNDING INFORMATION

This work was supported by the Co-operative Institute for Modeling the Earth System (CIMES), Princeton University/NOAA GFDL.

DATA AVAILABILITY STATEMENT

The analysis and plots that were generated for this work are accessible in the form of Jupyter Notebooks at https://doi.org/10.5281/zenodo.7908479.

ORCID

Cameron G. MacDonald https://orcid.org/0000-0003-2459-2808

REFERENCES

Adames, Á.F. & Kim, D. (2016) The MJO as a dispersive, convectively coupled moisture wave: Theory and observations. *Journal of the Atmospheric Sciences*, 73, 913–941.

Adames, Á.F., Kim, D., Clark, S.K., Ming, Y. & Inoue, K. (2019) Scale analysis of moist thermodynamics in a simple model and the relationship between moisture modes and gravity waves. *Journal of the Atmospheric Sciences*, 76, 3863–3881.

Adames, A.F. & Maloney, E.D. (2021) Moisture mode theory's contribution to advances in our understanding of the Madden-Julian oscillation and other tropical disturbances. *Current Climate Change Reports*, 7, 72–85.

Adames, Á.F. & Ming, Y. (2018) Interactions between water vapor and potential vorticity in synoptic-scale monsoonal disturbances: Moisture vortex instability. *Journal of the Atmospheric Sciences*, 75, 2083–2106.

Ahmed, F. (2021) The MJO on the equatorial beta plane: An eastward-propagating Rossby wave induced by meridional moisture advection. *Journal of the Atmospheric Sciences*, 78, 3115–3135.

Ahmed, F., Neelin, J.D. & Adames, Á.F. (2021) Quasi-equilibrium and weak temperature gradient balances in an equatorial beta-plane model. *Journal of the Atmospheric Sciences*, 78, 209–227.

Bender, C.M. & Orszag, S.A. (2013) *Advanced mathematical methods for scientists and engineers I: Asymptotic methods and perturbation theory*. New York: Springer Science & Business Media.

Boyd, J.P. (1978) The effects of latitudinal shear on equatorial waves. Part I: Theory and methods. *Journal of Atmospheric Sciences*, 35, 2236–2258.

Bretherton, C.S. & Smolarkiewicz, P.K. (1989) Gravity waves, compensating subsidence and detrainment around cumulus clouds. *Journal of Atmospheric Sciences*, 46, 740–759.

Briggs, R.J. (1964) *Electron-stream interaction with plasmas*, Vol. 187. MA: MIT Press Cambridge.

Chen, G. & Wang, B. (2018) Does the MJO have a westward group velocity? *Journal of Climate*, 31, 2435–2443.

Diaz, M. & Aiyyer, A. (2015) Absolute and convective instability of the African easterly jet. *Journal of the Atmospheric Sciences*, 72, 1805–1826.

Durran, D.R. (2013) *Numerical methods for wave equations in geophysical fluid dynamics*, Vol. 32. New York: Springer Science & Business Media.

Emanuel, K. (2020) Slow modes of the equatorial waveguide. *Journal of the Atmospheric Sciences*, 77, 1575–1582.

Emanuel, K.A., David Neelin, J. & Bretherton, C.S. (1994) On large-scale circulations in convecting atmospheres. *Quarterly Journal of the Royal Meteorological Society*, 120, 1111–1143.

Farrell, B.F. (1982) Pulse asymptotics of the Charney baroclinic instability problem. *Journal of Atmospheric Sciences*, 39, 507–517.

Fuchs, Ž. & Raymond, D.J. (2017) A simple model of intraseasonal oscillations. *Journal of Advances in Modeling Earth Systems*, 9, 1195–1211.

Fuchs-Stone, Ž. & Emanuel, K. (2022) Sensitivity of linear models of the Madden–Julian Oscillation to convective representation. *Journal of the Atmospheric Sciences*, 79, 1575–1584.

Fulton, S.R. & Schubert, W.H. (1985) Vertical normal mode transforms: theory and application. *Monthly Weather Review*, 113, 647–658.

Gaster, M. (1968) Growth of disturbances in both space and time. *The Physics of Fluids*, 11, 723–727.

Held, I.M. (2019) 100 years of progress in understanding the general circulation of the atmosphere. *Meteorological Monographs*, 59, 1–6.

Hendon, H.H. & Salby, M.L. (1994) The life cycle of the Madden–Julian oscillation. *Journal of Atmospheric Sciences*, 51, 2225–2237.

Huerre, P. & Monkewitz, P.A. (1985) Absolute and convective instabilities in free shear layers. *Journal of Fluid Mechanics*, 159, 151–168.

Huerre, P. & Monkewitz, P.A. (1990) Local and global instabilities in spatially developing flows. *Annual Review of Fluid Mechanics*, 22, 473–537.

Inoue, K. & Back, L.E. (2017) Gross moist stability analysis: Assessment of satellite-based products in the GMS plane. *Journal of the Atmospheric Sciences*, 74, 1819–1837.

Inoue, K., Biasutti, M. & Fridlind, A.M. (2021) Evidence that horizontal moisture advection regulates the ubiquitous amplification of rainfall variability over tropical oceans. *Journal of the Atmospheric Sciences*, 78, 529–547.

Jiang, X., Adames, Á.F., Kim, D., Maloney, E.D., Lin, H., Kim, H. et al. (2020) Fifty years of research on the Madden-Julian oscillation: recent progress, challenges, and perspectives. *Journal of Geophysical Research: Atmospheres*, 125, e2019JD030911.

Kiladis, G.N., Wheeler, M.C., Haertel, P.T., Straub, K.H. & Roundy, P.E. (2009) Convectively coupled equatorial waves. *Reviews of Geophysics*, 47, RG2003.

Kim, J.-E. & Zhang, C. (2021) Core dynamics of the MJO. *Journal of the Atmospheric Sciences*, 78, 229–248.

Lin, J.-L., Zhang, M. & Mapes, B. (2005) Zonal momentum budget of the Madden–Julian oscillation: The source and strength of equivalent linear damping. *Journal of the Atmospheric Sciences*, 62, 2172–2188.

Lin, S. & Pierrehumbert, R.T. (1993) Is the midlatitude zonal flow absolutely unstable? *Journal of Atmospheric Sciences*, 50, 505–517.

MacDonald, C.G. & Ming, Y. (2022) Tropical intraseasonal variability response to zonally asymmetric forcing in an idealized moist GCM. *Journal of Climate*, 35, 4479–4501.

Majda, A.J. & Stechmann, S.N. (2011) Nonlinear dynamics and regional variations in the MJO skeleton. *Journal of the Atmospheric Sciences*, 68, 3053–3071.

Maloney, E.D. (2009) The moist static energy budget of a composite tropical intraseasonal oscillation in a climate model. *Journal of Climate*, 22, 711–729.

Maloney, E.D., Sobel, A.H. & Hannah, W.M. (2010) Intraseasonal variability in an aquaplanet general circulation model. *Journal of Advances in Modeling Earth Systems*, 2, 5.

Maloney, E.D. & Wolding, B.O. (2015) Initiation of an intraseasonal oscillation in an aquaplanet general circulation model. *Journal of Advances in Modeling Earth Systems*, 7, 1956–1976.

Matthews, A.J. (2008) Primary and successive events in the Madden–Julian oscillation. *Quarterly Journal of the Royal Meteorological Society: A Journal of the Atmospheric Sciences, Applied Meteorology, and Physical Oceanography*, 134, 439–453.

Mayta, V.C. & Adames, Á.F. (2023) Moist thermodynamics of convectively coupled waves over the western hemisphere. *Journal of Climate*, 36, 2765–2780.

Mayta, V.C. & Adames Corraliza, Á.F. (2023) Is the Madden-Julian oscillation a moisture mode? *Geophysical Research Letters*, 50, e2023GL103002. Available from: https://doi.org/10.1029/2023GL103002

Merkine, L.-O. (1977) Convective and absolute instability of baroclinic eddies. *Geophysical and Astrophysical Fluid Dynamics*, 9, 129–157.

Merkine, L.-O. & Shafranek, M. (1980) The spatial and temporal evolution of localized unstable baroclinic disturbances. *Geophysical and Astrophysical Fluid Dynamics*, 16, 175–206.

Neelin, J.D. & Yu, J.-Y. (1994) Modes of tropical variability under convective adjustment and the Madden–Julian oscillation. Part I: Analytical theory. *Journal of Atmospheric Sciences*, 51, 1876–1894.

Pierrehumbert, R. (1984) Local and global baroclinic instability of zonally varying flow. *Journal of Atmospheric Sciences*, 41, 2141–2162.

Pierrehumbert, R.T. (1986) Spatially amplifying modes of the Charney baroclinic-instability problem. *Journal of Fluid Mechanics*, 170, 293–317.

Powell, S.W. & Houze, R.A., Jr. (2015) Effect of dry large-scale vertical motions on initial MJO convective onset. *Journal of Geophysical Research: Atmospheres*, 120, 4783–4805.

Ray, P. & Li, T. (2013) Relative roles of circumnavigating waves and extratropics on the MJO and its relationship with the mean state. *Journal of the Atmospheric Sciences*, 70, 876–893.

Raymond, D.J. & Fuchs, Ž. (2009) Moisture modes and the Madden–Julian oscillation. *Journal of Climate*, 22, 3031–3046.

Raymond, D.J. & Fuchs, Ž. (2018) The Madden-Julian Oscillation and the Indo-Pacific Warm Pool. *Journal of Advances in Modeling Earth Systems*, 10, 951–960.

Roundy, P.E. (2012a) Observed structure of convectively coupled waves as a function of equivalent depth: Kelvin waves and the

Madden–Julian oscillation. *Journal of the Atmospheric Sciences*, 69, 2097–2106.

Roundy, P.E. (2012b) The spectrum of convectively coupled Kelvin waves and the Madden–Julian oscillation in regions of low-level easterly and westerly background flow. *Journal of the Atmospheric Sciences*, 69, 2107–2111.

Rupp, P.M. & Haynes, P.H. (2020) Spatio-temporal stability analysis applied to monsoon anticyclone flow. *Quarterly Journal of the Royal Meteorological Society*, 146, 1861–1879.

Simmons, A.J. & Hoskins, B.J. (1979) The downstream and upstream development of unstable baroclinic waves. *Journal of the Atmospheric Sciences*, 36, 1239–1254.

Sobel, A. & Kim, D. (2012) The MJO-Kelvin wave transition. *Geophysical Research Letters*, 39, L20808.

Sobel, A. & Maloney, E. (2012) An idealized semi-empirical framework for modeling the Madden–Julian oscillation. *Journal of the Atmospheric Sciences*, 69, 1691–1705.

Sobel, A. & Maloney, E. (2013) Moisture modes and the eastward propagation of the MJO. *Journal of the Atmospheric Sciences*, 70, 187–192.

Sobel, A.H., Nilsson, J. & Polvani, L.M. (2001) The weak temperature gradient approximation and balanced tropical moisture waves. *Journal of the Atmospheric Sciences*, 58, 3650–3665.

Wang, S. & Sobel, A.H. (2022a) A unified moisture mode theory for the Madden–Julian Oscillation and the boreal summer intraseasonal oscillation. *Journal of Climate*, 35, 1267–1291.

Wang, S. & Sobel, A.H. (2022b) A filtered model for the tropical intraseasonal moisture mode. *Geophysical Research Letters*, 49, e2022GL098320.

Wang, S., Tan, Z.-M., Wu, Z. & Fang, J. (2022) Moisture modes of tropical intraseasonal oscillations—high order and anti-symmetric solutions. *Journal of Geophysical Research: Atmospheres*, 127, e2021JD036413.

Wei, Y., Ren, H.-L., Xiang, B., Wang, Y., Wu, J. & Wang, S. (2023) Diverse MJO Genesis and Predictability. *Bulletin of the American Meteorological Society*, 104, E792–E809.

Zhang, C., Adames, Á., Khouider, B., Wang, B. & Yang, D. (2020) Four theories of the Madden-Julian oscillation. *Reviews of Geophysics*, 58, e2019RG000685.

Zhao, C., Li, T. & Zhou, T. (2013) Precursor signals and processes associated with MJO initiation over the tropical Indian Ocean. *Journal of Climate*, 26, 291–307.

How to cite this article: MacDonald, C.G. (2024) Absolute instability of moisture-coupled waves on the equatorial beta-plane. *Quarterly Journal of the Royal Meteorological Society*, 150(762), 2667–2689. Available from: https://doi.org/10.1002/qj.4728

APPENDIX. DERIVATION OF THE DISPERSION RELATION WITH NON-ZERO MERIDIONAL WIND

Here we show in detail how the meridional structure equation and dispersion relation for a system with a non-zero meridional wind are derived from the governing equations. Equation (4c) gives the following expression for $\langle q\rangle$:

$$\langle q\rangle = \frac{\tau_\mathrm{c}}{1+r}\left(i\sigma\frac{M_\mathrm{s}}{c^2}\phi_1 - ikM_\mathrm{s}u_1 - M_\mathrm{s}\frac{dv_1}{dy}\right). \tag{A1}$$

This may be used to eliminate $\langle q\rangle$ from Equation (4d). Defining $\sigma_\mathrm{c} \equiv \sigma + i\tau_\mathrm{c}^{-1}$, we get

$$C_0\phi_1 + C_1u_1 + C_2yv_1 + C_3\frac{dv_1}{dy} = 0, \tag{A2}$$

where the coefficients are

$$C_0 = \sigma\sigma_\mathrm{c}\frac{M_\mathrm{s}\tau_\mathrm{c}}{c^2(1+r)}, \tag{A3a}$$

$$C_1 = -\sigma_\mathrm{c}k\frac{M_\mathrm{s}\tau_\mathrm{c}}{1+r} + A_q + ikM_q, \tag{A3b}$$

$$C_2 = -B_q, \tag{A3c}$$

$$C_3 = M_q + i\sigma_\mathrm{c}\frac{M_\mathrm{s}\tau_\mathrm{c}}{1+r}. \tag{A3d}$$

Using Equations (4a) and (4b), the following identities may be formed to eliminate u_1 and ϕ_1 in favour of v_1:

$$u_1 = \frac{k}{\sigma}\phi_1 + i\frac{\beta}{\sigma}yv_1, \tag{A4a}$$

$$\left(k\frac{d}{dy} + \frac{k^2\beta y}{\sigma}\right)\phi_1 = -i\frac{k\beta^2}{\sigma}y^2v_1. \tag{A4b}$$

After the application of these identities, we obtain the meridional structure equation for v_1,

$$\frac{d^2v_1}{dy^2} + D_0y\frac{dv_1}{dy} + (D_1 + D_2y^2)v_1 = 0, \tag{A5}$$

where the $D_{(\cdot)}$ coefficients are given in Section 4.2. To derive the dispersion relation, we transform this equation into its canonical Schrödinger form (Boyd, 1978). The dependent variable is changed to

$$V = v_1\exp\left(\int\frac{D_0y^*}{2}dy^*\right) = v_1\exp(D_0y^2/4), \tag{A6}$$

and the independent variable to

$$\xi = (D_1 - D_0/2)^{1/4}y. \tag{A7}$$

The governing equation then has the form

$$\frac{d^2V}{d\xi^2} + (E_0 - \xi^2)V = 0, \tag{A8}$$

where $E_0 = (D_1 - D_0/2)/\sqrt{D_0^2/4 - D_2}$. Equation (A8) is of the desired canonical form and has solutions satisfying

$$E_0 = 2n + 1, \tag{A9a}$$

$$V_n(\xi) = e^{-\xi^2/2} H_n(\xi), \tag{A9b}$$

where H_n are Hermite polynomials and n is a positive integer. After substitution of the definition for E_0, Equation (A9a) gives the dispersion relation stated in the main text; the real part of Equation (A9b), when written in terms of v_1 and y, provides the equatorial trapping condition.